



University of Potsdam
Institute of Geoscience

Master's thesis

**Generating high-resolution DEMs from
tri-stereo satellite imagery:
A geomorphologic case study in the
Quebrada del Toro, NW Argentina**

by

Ariane Müting

Supervisors

Prof. Dr. Bodo Bookhagen
Prof. Manfred R. Strecker, PhD

Potsdam, 30.03.2020

Hiermit versichere ich, Ariane Müting, dass ich die vorliegende Arbeit selbstständig und ohne Benutzung anderer als der von mir angegebenen Quellen angefertigt habe. Sämtliche Bereiche der Arbeit, die diese Quellen und Hilfsmittel dem Wortlaut oder dem Sinne nach wiedergeben, sind als solche kenntlich gemacht und im Quellenverzeichnis aufgeführt.

Ich versichere weiterhin, dass diese Arbeit weder in der vorliegenden Fassung, noch in einer abgewandelten Form bereits zu einer anderen Prüfung vorgelegt wurde. Die „Richtlinie zur Sicherung guter wissenschaftlicher Praxis für Studierende an der Universität Potsdam“ (Plagiatsrichtlinie) vom 20. Oktober 2010 ist mir bekannt.

Potsdam, 30. März 2020

Zusammenfassung

Die meter-genaue Auflösung der Erdoberfläche ist für ein besseres Verständnis der topographischen Besonderheiten von Murgängen in steilen Gebirgsregionen von entscheidender Bedeutung. In Gegenden mit hohem Relief stellt das Sammeln zuverlässiger Informationen über die Beschaffenheit der Oberflächenstruktur jedoch eine Herausforderung dar. Diese Studie erforscht das Potenzial von Stereogrammetrie zur Erstellung digitaler Höhenmodelle (DEMs) auf der Grundlage hochauflösender Satellitenbilder für die östlichen Andenkordillern von NW-Argentinien. Durch den Vergleich mit Bodenkontrolldaten und die visuelle Bewertung der Ergebnisse identifiziere ich die optimalen Parameter für die Erzeugung von DEMs in Hochreliefgebieten unter Verwendung von SPOT-7 tri-stereo Daten. Meine Ergebnisse zeigen, dass steiles Gelände durch stereogrammetrische Methoden deutlich besser abzubilden ist, als es durch Radarinterferometrie erzeugte DEMs vermögen. Eine sorgfältige Datenvor- und -nachbearbeitung ist dennoch unerlässlich, um optimale Ergebnisse zu erzielen. Hochauflösende DEMs ermöglichen es, die topographische Signatur von Murgängen zu identifizieren. Vorangegangene Studien haben gezeigt, dass Murgänge eine andere Beziehung von Gefälle und Wassereinzugsgebiet in logarithmischer Darstellung aufweisen, als fluvial geprägte Flusssysteme. Diese Studie liefert weitere Hinweise für dieses Phänomen aus dem Nordwesten Argentinien. Mit Hilfe der einzigartigen topographischen Signatur von Murgängen ist es möglich, räumliche Variationen der vorherrschenden Transportprozesse im Einzugsgebiet des Río Toro aufzudecken und die Ausmaße von Murgängen einzugrenzen. Diese neuen Ergebnisse deuten auf eine erhöhte Murgangintensität innerhalb der tief eingeschnittenen Schlucht im südlichen Bereich und entlang der Ostflanke des Toro Beckens hin. Es lässt sich feststellen, dass ein hohes Relief, welches mit aktiven Störungen korrespondiert, die Hauptursache für Murgangaktivität im Einzugsgebiet des Río Toros ist. Die Murgangaktivität korrespondiert zudem mit Regionen spärlicher Vegetationsbedeckung und schwach metamorphem Grundgestein. Diese Ergebnisse ermöglichen eine verbesserte Einschätzung der Gefährdung durch Murgänge in der Quebrada del Toro, was bei weiterführender Infrastrukturplanung in dieser Region berücksichtigt werden sollte.

Abstract

Resolving Earth's surface at the meter scale is essential for an improved understanding of the topographic peculiarities that originate from debris-flow activity in mountainous high-relief terrains. Obtaining reliable information on the surface structure in these regions is challenging. In this study, I explore the potential of stereogrammetry for creating digital elevation models (DEMs) based on high-resolution satellite imagery for the Eastern Andean Cordillera of NW Argentina, an area with extreme gradients in topography, rainfall, and erosion. Through comparison with ground-control data and visual output assessment, I identify the optimal parameters for DEM generation in high-relief areas using SPOT-7 tri-stereo satellite imagery. I find that stereogrammetry is better suited to depict steep terrain than DEMs created from radar interferometry as surface distortions related to the side-looking geometry of the sensor are omitted. Careful data pre- and post-processing is, however, vital for obtaining optimal results. The topographic signature of debris flows can further be elaborated using high-resolution high-accuracy DEMs. Debris flows have been shown to deviate from the power-law relationship of topographic slope and drainage area that is commonly used to describe river incision. I provide further evidence for this phenomenon from the Eastern Andean Cordillera. Employing the distinctive topographic signature of debris flows, I am able to uncover spatial variations of dominating transport processes within the catchment of the Río Toro and constrain initiation areas of debris flow. My new results suggest increased debris-flow intensity within the deeply entrenched gorge of the Toro river and along the eastern flank of the basin. Slope associated with active faulting is identified to be the major driver of debris flow within the catchment. Debris flow activity further corresponds with regions of sparse vegetation cover and exposure of cataclacized bedrock. These findings are critical for an improved assessment of hazard from debris flow in the Quebrada del Toro, which should be taken into consideration for further infrastructural planning and development.

Contents

1. Introduction	1
2. Study area	4
3. Data	6
3.1. Satellite imagery	6
3.2. Ground-control data	6
4. Methods	8
4.1. DEM generation	8
4.1.1. Bundle adjustment	8
4.1.2. Map-projection	9
4.1.3. Stereo correlation	9
4.1.4. Point-cloud alignment	9
4.1.5. DEM filtering	10
4.2. DEM Analysis	10
4.2.1. Extracting the topographic signature of debris flows	10
4.2.2. Automated debris-flow detection	12
4.2.3. From catchments to squares	16
4.2.4. Debris-flow detection on TanDEM-X data	18
4.2.5. Computing debris-flow intensity	20
5. Results	22
5.1. DEM quality	22
5.2. Debris-flow intensity derived from high-resolution DEMs	26
5.3. Debris-flow intensity from TanDEM-X data	28
6. Discussion	32
6.1. Stereogrammetry as a tool for DEM generation	32
6.2. Potential of ground-control data	33
6.3. Challenges of debris-flow detection	34

Contents

6.4. Factors triggering debris-flow activity	35
7. Conclusion	43
A. Appendix	45
A.1. Peculiarities of topographic signatures from different catchment types	45
A.2. Further assessment of DEM quality	47
A.3. DEMs from Cartosat-1	48

List of Figures

1.1. Hypothetical slope against drainage-area plot of different hillslope and valley processes. Adapted from (Stock and Dietrich, 2003).	2
2.1. Detailed view of the study area in the southeastern Central Andes in NW Argentina showing steep gradients in topography (A), slope (B), and vegetation cover (C) (courtesy of Bodo Bookhagen).	4
3.1. Extent of SPOT-7 data and location of kinematic dGPS points (orange) and static ground control points (red).	7
4.1. Error distribution and filter threshold for QdT (A) and Capilla dataset (B).	11
4.2. Filtering effects on topographic slope for QdT (A) and Capilla dataset (B).	11
4.3. Relation between topographic slope and drainage area in log-log space for three exemplary control basins with the imposed classification (A) and the interpretation of dominating geomorphic processes according to (Stock and Dietrich, 2003) (B).	13
4.4. Hand-classified control catchments within the extent of the 3 m stereo DEM.	14
4.5. θ -values of the initial linear fit separated by basin type with threshold employed in basin classification (A) and adjusted R^2 values of the initial linear fit to $\log S$ against $\log A$. Shaded areas indicate IQR.	15
4.6. Difference in θ values of first (debris flow) and second (fluvial) slope segments fitted to the $\log S$ $\log A$ relation for basins classified as debris flow or fluvially dominated (A) and mixed basins (B). Shaded areas indicate IQR.	15
4.7. Schematic overview of the steps involved in the automatic debris-flow detection.	16
4.8. Auto-classified test basins with topographic information and thresholds from 3 m stereo DEM (A) and TanDEM-X (B).	17

List of Figures

4.9. Confusion matrices comparing results of manual classification with auto classification using topographic information and thresholds from 3 m stereo DEM (A) and TanDEM-X (B). Columns represent the manual assigned classes from the reference data set, rows indicate the automatically assigned classes.	18
4.10. Relation between topographic slope and drainage area in log-log space for three exemplary control basins with values extracted from 12 m TanDEM-X (A) and 30 m SRTM (B).	19
4.11. θ thresholds for basin classification based on TanDEM-X data. Difference between θ of a single fitted regression line (A) and θ values for first and second slope segments of mixed basins (B). Shaded areas indicate IQR.	21
4.12. Topographic signature and θ values of two exemplary squares covering low-sloping alluvial-fan deposits in the upper reaches of the Rio Toro catchment.	21
5.1. Comparison of original TanDEM-X DEM (A) to stereo DEM map-projected onto TanDEM-X (B), stereo DEM map-projected onto low-resolution DEM created with ASP (C) and stereo DEM map-projected onto 90 m SRTM (D).	23
5.2. Difference of stereo DEMs to kinematic dGPS points, comparing initial results of bundle adjustment with and without GCPs (A) and the aligned DEM, bundle adjusted with GCPs vs. a DEM created without any ground control (B). Shaded areas indicate IQR.	24
5.3. Comparing the results of DEMs that were created using parabola fitting (A), an affine adaptive window with Bayes EM weighting (B) and an affine window only (C) during subpixel refinement.	25
5.4. Visual assessment of DEMs created with different kernel sizes during the stereo-correlation process. 11 x 11 pixel (A) 15 x 15 pixel (B) 21 x 21 pixel (C).	25
5.5. Debris-flow identification for QdT using high-resolution topographic data. Tiles cover an extent of 4 km ² and are colored by estimated breakpoint location (A). Extracted debris-flow pixels (B).	26

List of Figures

5.6. Normalized debris-flow intensity determined through quadtrat counting (A) and normalized kernel-smoothed intensity function (B) for QdT based on high-resolution topographic data. Blue stars indicate regions that stood out as debris-flow prone during the field campaign, portrayed in (C) and (D).	27
5.7. Comparing estimated locations of debris flows (A) to satellite imagery from Google Maps (B).	28
5.8. Normalized debris-flow intensity determined through quadtrat counting (A) and normalized kernel-smoothed intensity function (B) for QdT based on TanDEM-X data.	29
5.9. Results of breakpoint analysis based on TanDEM-X data (A) and absolute difference of breakpoint location compared to results from stereo DEM (B).	29
5.10. Classificating of 2 x 2 km squares covering the entire Rio Toro catchment (A) and location of detected breakpoint (B).	31
5.11. Normalized debris-flow intensity determined through quadtrat counting (A) and normalized kernel-smoothed intensity function (B) for the entire Rio Toro watershed based on TanDEM-X data.	31
6.1. DEM adjusted and aligned with ground control data differenced against a DEM created without any ground control (A) and TanDEM-X (B).	34
6.2. Maximum NDVI mosaic from Landsat 8 scenes aquired in October 2014 (A) and geologic map of the Quebrada del Toro indicating lithologic units and main fault strands adapted from Tofelde et al. (2017) (B) together with debris-flow intensity contour lines.	36
6.3. Possible relation between debris-flow intensity and vegetation cover.	37
6.4. Possible relation between debris-flow intensity and exposed rock type.	38
6.5. Possible relation between debris-flow intensity and distance to nearest fault segment. Debris-flow intensities are extracted at equally spaced sample point locations that are then investigated concerning their distance to the closest fault segment.	39
6.6. Map of the main fault segments within the QdT and surroundings together with localities of all earthquakes with a magnitude > 2.5 that occurred between 2000 and 2020.	40
6.7. Possible relation between debris-flow intensity and slope aspect.	41

List of Figures

A.1. Aggregated mean IQR of slope within drainage-area logbins for hand-classified basins with topographic information extracted from ASP DEM.	45
A.2. Aggregated mean IQR of slope within drainage-area logbins for auto-classified squares with topographic information extracted from ASP DEM (A) and IQR of hand-classified basins based on TanDEM-x data (B). Shaded areas indicate IQR of aggregated values.	46
A.3. Log S log A relation and IQR of two exemplary test basins.	46
A.4. Difference of stereo DEMs to kinematic dGPS points, comparing subpixel-mode (A), subpixel kernel (B), reference DEM for map-projection (C), and number of GCPs used for bundle adjustment (D).	47
A.5. Visual assessment of DEM created from SPOT-7 data (A) compared to results from Cartosat-1 (B), generated with the same input parameters for stereo correlation.	49

1. Introduction

Mountainous high-relief terrains in climatically sensitive regions are often subjected to natural extreme events such as debris flows and landsliding. With people and infrastructure at risk, it is important to identify, measure, and comprehend the driving forces and mechanisms of slope movements in these environments at a regional scale. Geomorphological analyses and hazard assessments in these regions are, however, often limited by the availability of good-quality high-resolution digital elevation models (DEMs). Publicly available DEMs derived from radar interferometry often have lower spatial resolution and are distorted in high-relief areas. In contrast, airplane-based light detection and ranging (lidar) data provide highly accurate information on 3D structure, yet, the acquisition is costly and limits the size of the respective study area. Finding adequate, economical alternatives for creating high-resolution DEMs is therefore essential to study Earth-surface processes at the regional scale, which may enable the detection of spatial variations, clusters, and trends.

In areas with sparse vegetation, stereogrammetry has proven to be a viable tool for creating high-resolution DEMs (e.g., Tao et al. (2018), Shean et al. (2019)). Stereogrammetry is using optical data to extract 3D spatial information from two or more overlapping images. Satellite imagery can easily be acquired over larger areas, and inferred DEMs have a spatial resolution in the range of a few meters. Stereo images are either freely available upon request or cost a fraction of the lidar data for comparable coverage. Thus, stereogrammetry has the potential to bridge the gap between radar and lidar-inferred surface structure in terms of resolution and feasibility.

In this study, I explore the opportunities of high-resolution stereo DEMs for geomorphic applications in the Eastern Cordillera of the NW Argentine Andes, an area with extreme gradients in topography, rainfall, and erosion. Field observations in this area have shown that debris flows of various extents characterize the hillslopes of the deeply incised gorges connecting the lowland with the Puna plateau in the interior of the Andean orogen (e.g., Cencetti and Rivelli (2011), Wayne (2011)). Debris flows pose a severe threat to infrastructure and human lives in high-relief regions all around the globe. Hence, a better understanding of the signature and driving factors of slope

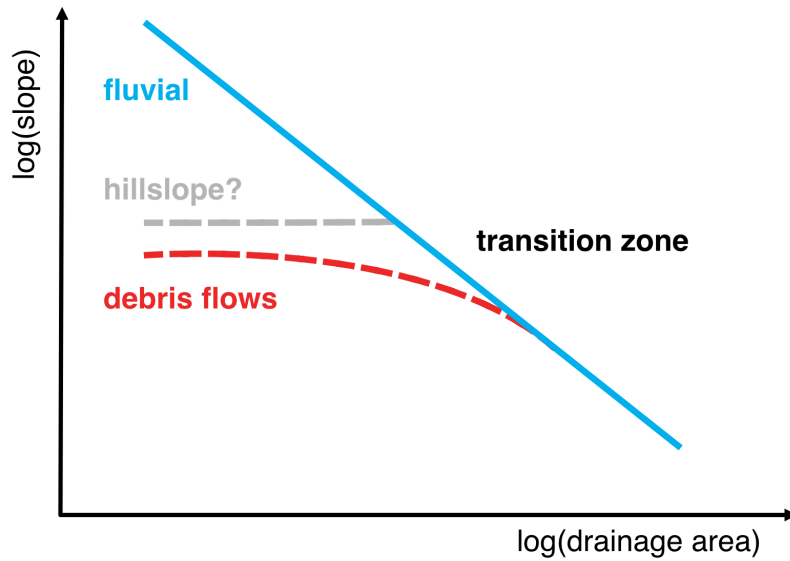


Figure 1.1.: Hypothetical slope against drainage-area plot of different hillslope and valley processes. Adapted from (Stock and Dietrich, 2003).

movements is crucial for thoughtful planning and appropriate risk management. Debris flows are gravity-induced mass movements of poorly sorted, water-saturated sediment (Iverson, 1997). Although debris flows ordinarily originate at high slopes, their fluidity enables the inundation of wide areas, depending on the transported sediment and water content. Debris flows have stood out in past studies as they do not follow the power-law relationship between local topographic slope and drainage area (e.g., Seidl and Dietrich (1992), Montgomery and Foufoula-Georgiou (1993), Stock and Dietrich (2003), Santos and Duarte (2006)). This power-law relationship is well documented for channels dominated by fluvial processes where the change in channel gradient can generally be expressed as

$$S = k_s A^{-\theta} \quad (1.1)$$

where S is the slope, A the upstream drainage area, θ a measure for the concavity of the channel profile, and k_s the steepness index (Flint, 1974). Logarithmizing this equation indicates a linear relationship between drainage area and channel gradient with θ as slope and k_s as the y-intercept. Debris flows, however, show a different relationship. Stock and Dietrich (2003) found that the stream-power law does not extend to slopes greater than 0.03 - 0.10. At steep slopes, channel incision can often be attributed to episodic debris-flow scour, which has a different relationship of $\log S$

1. Introduction

against $\log A$, ultimately leading to a curved relationship in log-log space (Stock and Dietrich, 2003) (Figure 1.1). This finding has led to the conclusion that the simple stream-power law, which is frequently applied to model river incision, is incomplete. Therefore, it might not accurately describe the evolution of mountainous high-relief areas that exhibit widespread debris-flow activity (Stock et al. (2005), Stock and Dietrich (2006)).

In this study, I use the deviation of debris flows from the conventional power-law relationship between slope and drainage area to identify the predominant agent of sediment transport within different regions of my study area. Thereby, it is possible to distinguish regions that are particularly prone to slope movements. Using high-resolution topographic data, I am able to further characterize the distinct topographic signature of debris flows and relate them to local environmental conditions. These observations help to better understand the formation of large volumes of sediment in a semi-arid, mountainous environment.

2. Study area

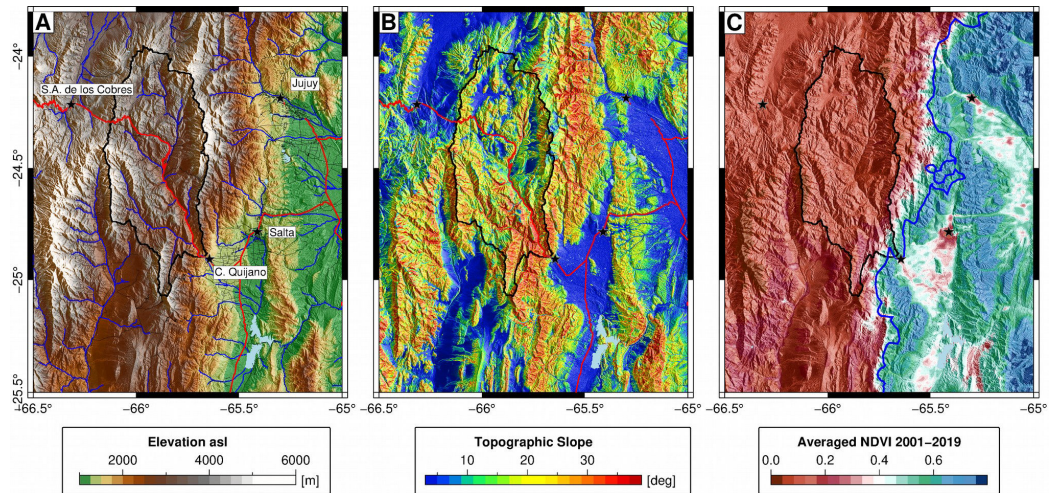


Figure 2.1.: Detailed view of the study area in the southeastern Central Andes in NW Argentina showing steep gradients in topography (A), slope (B), and vegetation cover (C) (courtesy of Bodo Bookhagen).

The Eastern Cordillera of NW Argentina is an area characterized by extreme gradients in topography, rainfall, erosion, and seismicity (Figure 2.1). The mountain range connects the arid Altiplano-Puna plateau at an average elevation of 3700 m with the more humid foreland at about 1100 m above sea-level (Strecker et al., 2007). The Eastern Andean Cordillera is a Cenozoic thrust-belt differentiated by several fault-bounded basins, which are essential pathways for infrastructure. The two main routes linking the plateau with the more populated lowlands traverse the deeply entrenched Quebrada del Toro (QdT) and Quebrada del Escoipe. High relief, recurring seismic activity, and infrequent rainstorm events during the South American summer monsoon make these valleys particularly susceptible to debris-flow activity (Wayne, 2011).

The QdT is a reverse fault-bounded basin located at $\sim 24.5^{\circ}\text{S}$ southwest of the city of Salta that has been actively deforming since the Miocene (Hilley and Strecker, 2005).

2. Study area

To the north, the valley exhibits relatively flat terrain that consists of highly erodible Tertiary and Quaternary conglomeratic terrace deposits. At the same time, the South is dominated by Precambrian through Paleozoic basement rocks (Hilley and Strecker (2005), Tofelde et al. (2017)). The incision of the Toro river has created a steep, narrow gorge in the lower parts of the Toro catchment, which is frequently impacted by debris-flow activity (Cencetti and Rivelli (2011), Wayne (2011)). Persistent mass wasting from nearby hillslopes and contributing catchments has led to river-bed aggradation, which is associated with the risk of flooding, loss of agricultural land, and temporary blockage of the mainstream. Due to the sustained sediment input, the main route leading through the QdT requires permanent, costly maintenance in the form of longitudinal defense work or excavation of the river bed.

Climatically, the QdT is situated in a semi-arid region. Like the entire Eastern Andean Cordillera, a pronounced orographic rainfall gradient characterizes the basin (Strecker et al., 2007). Rainfall measurements range from ~ 900 mm/yr at the outlet of the basin to < 200 mm/yr in the interior of the catchment (Tofelde et al., 2017), leading to a distinct change in vegetation cover: while a dense forest covers the Eastern flank of the Quebrada, vegetation coverage rapidly declines westwards, offering ideal conditions for stereogrammetric surface reconstruction.

3. Data

3.1. Satellite imagery

DEMs are created from panchromatic, cloud-free tri-stereo SPOT-7 satellite imagery at a resolution of 1.5 m covering the lower part of the QdT and Río Capilla catchment, a tributary to the Toro river. As the Río Capilla extension was purchased after the initial dataset for the QdT, both regions require individual processing, even though they belong to the same scene collected in October 2014. In addition, I work with Cartosat-1 stereo-pairs, covering the area of the Quebrada del Toro and Río Capilla at a resolution of 2.5 m to compare results from commercial and freely available data. (Indian satellite data have been made available upon request from the ESA).

3.2. Ground-control data

Ground-control measurements were taken during a field campaign in March 2019 to ensure spatial coherence and assess the vertical accuracy of my DEMs. In total, I collected 23 highly precise static dGPS points located at distinct features that would be well recognizable at 1.5 m resolution. These spots include bridges, road intersections, or railroad crossings within the extent of the aerial imagery. Static GPS points were measured for at least 10 minutes at a sampling rate of one point per second and then subsequently averaged. 16897 kinematic dGPS measurements with less than 0.5 m vertical and horizontal accuracies complement these stationary GPS points. The kinematic dGPS points were grouped by location to avoid bias from spatial clusters, leaving 4989 for the DEM accuracy assessment. Rough terrain and limited accessibility constrain the ground-control measurements to the area around the main road, which connects the cities of Campo Quijano and San Antonio de los Cobres.

3. Data

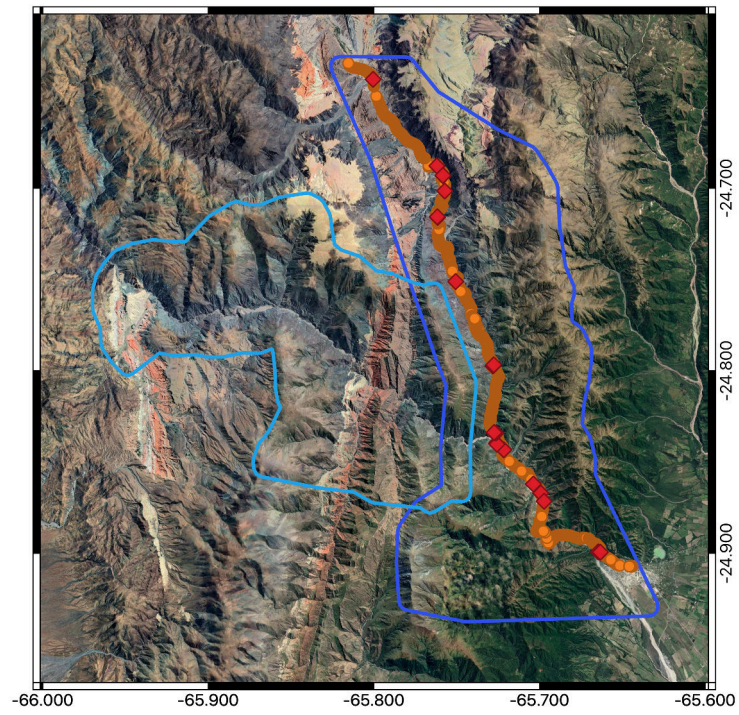


Figure 3.1.: Extent of SPOT-7 data and location of kinematic dGPS points (orange) and static ground control points (red).

4. Methods

This study consists of two parts. I first elaborate on the creation of high-resolution DEMs through stereogrammetry. The resulting stereo DEM serves as a basis for subsequent geomorphologic analyses that aim to identify debris flows within the QdT.

4.1. DEM generation

The 3D structure of an object or land surface can be determined by matching two or more photographs from different camera locations through stereo correlation. A program that enables fast and easy stereo correlation is Ames Stereo Pipeline (ASP). ASP is a collection of free and open-source geodesy and stereogrammetry tools designed for processing stereo images (Beyer et al., 2018). Next to the main stereo-correlation algorithm, the software facilitates data pre- and postprocessing, which is essential for minimizing errors. In this study, I use ASP to create high-resolution DEMs from tri-stereo SPOT-7 data. Obtaining optimal results require several processing step which I explain in more detail below.

4.1.1. Bundle adjustment

The first step preceding stereo correlation is bundle adjustment. Beyer et al. (2018) recommend this step to minimize satellite position and orientation errors, and avert systematic errors within the final DEM. Bundle adjustment ensures that the observations of a single ground feature within all input images are self-consistent by minimizing the disparity between the estimated, back-projected pixel locations and their actual locations in the captured images (Beyer et al., 2018). Bundle adjustment can benefit from ground-control points as they have the potential to improve the internal consistency of the output DEM and align it to the measured ground truth (Beyer et al., 2018). I test this potential by using 23 stationary GPS points in the bundle-adjustment process. Image coordinates are matched with actual GPS coordinates through manual clicking the ground-control points on the panchromatic satellite imagery. Uncertainties are assigned subjectively and amount to 2-5 pixels.

4. Methods

4.1.2. Map-projection

Map-projection is another pre-processing step that significantly improves DEM quality. It projects stereo pairs onto a pre-existing smooth DEM to enhance the images' similarity. This step aids the subsequent stereo correlation as the neighborhood of a pixel in the left image is more likely to be matched with a neighborhood in the right image (Beyer et al., 2018). I test different pre-existing terrain models as a basis for map-projection, namely SRTM at 30 m and 90 m resolution and TanDEM-X at 12 m resolution. Another way to obtain smooth DEM is from ASP directly by running stereo correlation and gridding the result to a very low resolution.

4.1.3. Stereo correlation

Stereo correlation is the primary tool of ASP. It takes stereo pairs and produces a 3D point cloud that can then be gridded to a DEM. The process has several stages. Fundamentally, two images are aligned, the correspondence between the pixels in the left and right image is computed, pixels are matched, followed by the determination of the 3D location of points through triangulation (Beyer et al., 2018). As I work with tri-stereo data, stereo correlation is performed for two sets of stereo pairs. One image represents the reference image, and the other two images are aligned and matched to that first image. Stereo correlation is carried out three times with the forward, backward, and nadir image as a reference to ensure that my choice of reference image does not influence the final DEM. Merging the resulting point clouds composes the final 3D surface.

4.1.4. Point-cloud alignment

When comparing ASP DEM and kinematic GPS points, it appears that even though the imagery is matched to the static GPS points during bundle adjustment, an offset of about 3 m remains between the two datasets. Thus, the point cloud obtained from stereo correlation is subsequently aligned to the ground control to ensure spatial coherence. For this step, however, more than the initial 23 static GPS points are needed, why I randomly divide the kinematic dGPS points into two sets – one for alignment and one for control purposes. After the initial alignment of the QdT segment to the ground control, the 3D point cloud covering the Río Capilla is aligned to the adjusted Toro point cloud, which is achievable due to a generous overlap of the SPOT-7 data. As a final step, the merged and aligned point cloud is gridded to a resolution of 3 m, which is equal to twice the resolution of the aerial imagery.

4. Methods

4.1.5. DEM filtering

To smooth out small irregularities and artifacts persisting after the stereo correlation, a lowpass filter with a kernel size of 3 x 3 pixels is applied to the final DEM. By using a filter threshold, only regions where correlation did not work well are altered, while successful correlation results remain untouched. This threshold is determined by the 75th percentile of the triangulation ray intersection error, separately for both the Río Toro and Río Capilla, as they show different error distributions (Figure 4.1). The ray intersection error is a metric estimated during the triangulation stage of the stereo correlation and is an indirect measure of DEM quality. High values indicate a low self-consistency of the DEM. Small areas with high triangulation error result from correlation mistakes, yet larger erroneous areas can point to camera-model inadequacies (Beyer et al., 2018).

Filtering principally affects regions with either very high or low slope values, as seen in Figure 4.2. Slightly extenuating very steep parts might moderately alter the results of subsequent geomorphic analyses, especially since steep sloping areas are prone to show debris-flow activity. Still, it is to expect that erroneous regions are not of great value for any analysis in the first place and can thus be smoothed with reasonable confidence.

4.2. DEM Analysis

This section concerns the extraction of regions within the QdT that have experienced debris-flow activity based high-resolution topographic data. The assumption going into this analysis is that debris-flow incision follows the characteristic $\log S \log A$ relation described by citestock03. The classification algorithm I present is established on the basis of several test basins in the lower part of the Toro basin and then subsequently extended to the entire catchment.

4.2.1. Extracting the topographic signature of debris flows

To get an overview of the relationship between local topographic slope and drainage area within the lower Río Toro Catchment, 68 control basins with a minimum size of one square kilometer are defined. Flow accumulation and slope in units of rise and run are calculated for each catchment. The multiplication of the flow accumulation with the pixel size results in the drainage area, which is assigned to logarithmic bins of different capacities. I iteratively increase the number of logbins, splitting the data first into 10, then 20, and up to 100 logbins to increase the number of

4. Methods

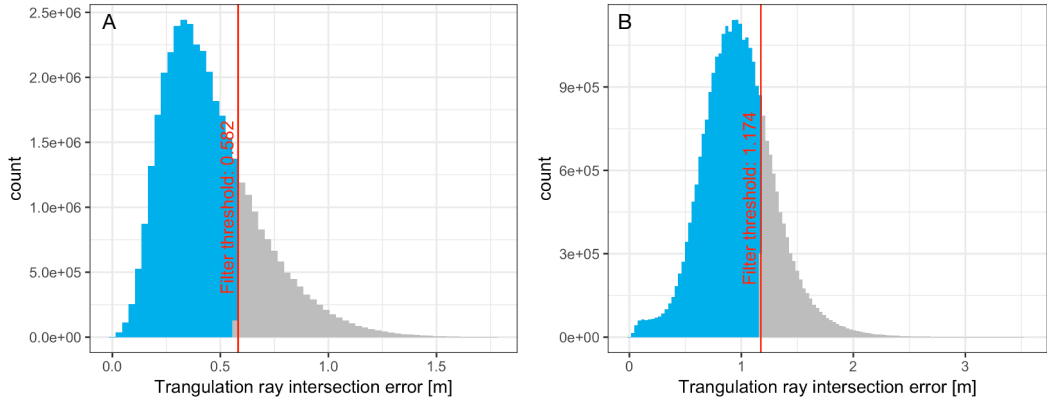


Figure 4.1.: Error distribution and filter threshold for QdT (A) and Capilla dataset (B).

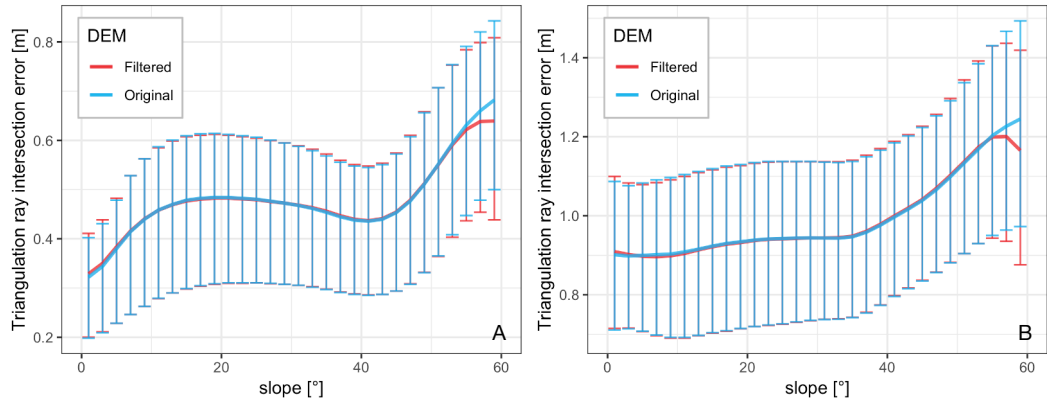


Figure 4.2.: Filtering effects on topographic slope for QdT (A) and Capilla dataset (B).

measurements and avoid any effects that may result from averaging slope values over too few bins, too many bins or just a single bin-size in general. Also, a lower drainage area threshold equal to 100 x pixel-size of the DEM is set to ensure the topographic analyses are limited to channelized areas. Finally, the median and interquartile range (IQR) of the slope are determined for every logbin.

Through plotting $\log S$ against $\log A$ for each basin individually, it emerges that the bend of the slope-area relation in log-log space described by Stock and Dietrich (2003) is a phenomenon that also exists in the East Andean Cordillera. However, I notice that the kink, supposedly marking the transition between debris flow and river incision, is not present in every test catchment. Based on these observations, I group my control catchments into three categories according to the interpretation of Stock and Dietrich (2003) (see Figure 1.1). I consider seven basins displaying no deviation

4. Methods

from the linear $\log S$ $\log A$ relation at drainage areas higher than 900 square meters to be dominated by fluvial processes. Nineteen basins without a clear kink-point, however, indicating a non-linear connection of $\log S$ against $\log A$ are interpreted to be debris-flow channels without any transition to fluvial incision before drainage areas greater than one square kilometer. Forty-two catchments manifesting a clear curved relationship with a non-linear (debris flow) and a linear (fluvial) segment in log-log space are attributed to a third, mixed class (Figure 4.3 and Figure 4.4).

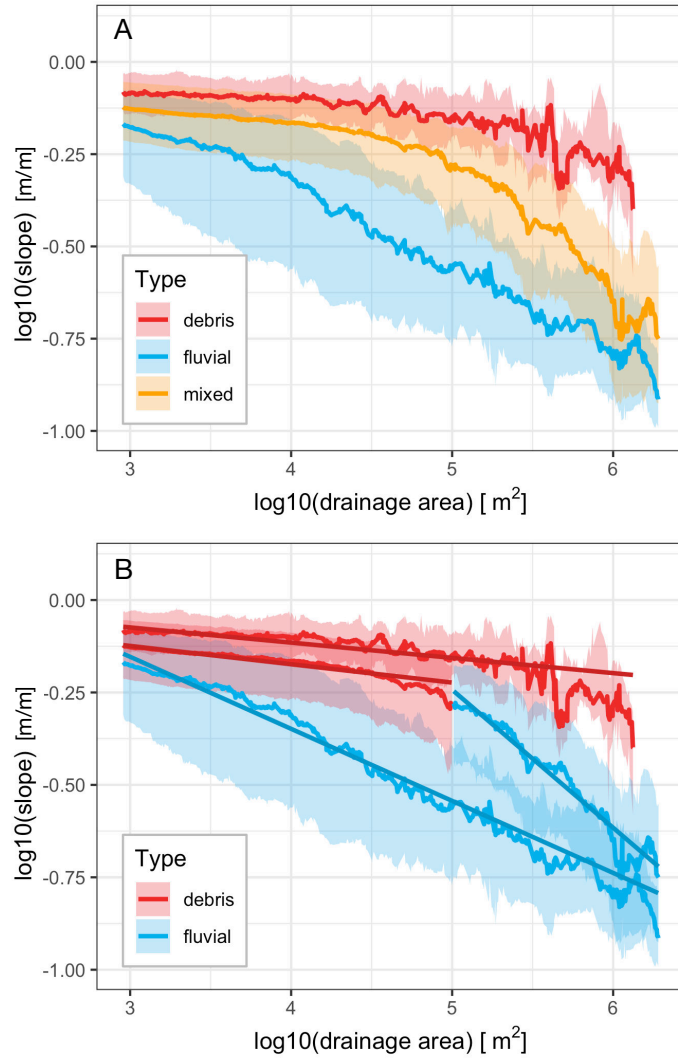


Figure 4.3.: Relation between topographic slope and drainage area in log-log space for three exemplary control basins with the imposed classification (A) and the interpretation of dominating geomorphic processes according to (Stock and Dietrich, 2003) (B).

4. Methods

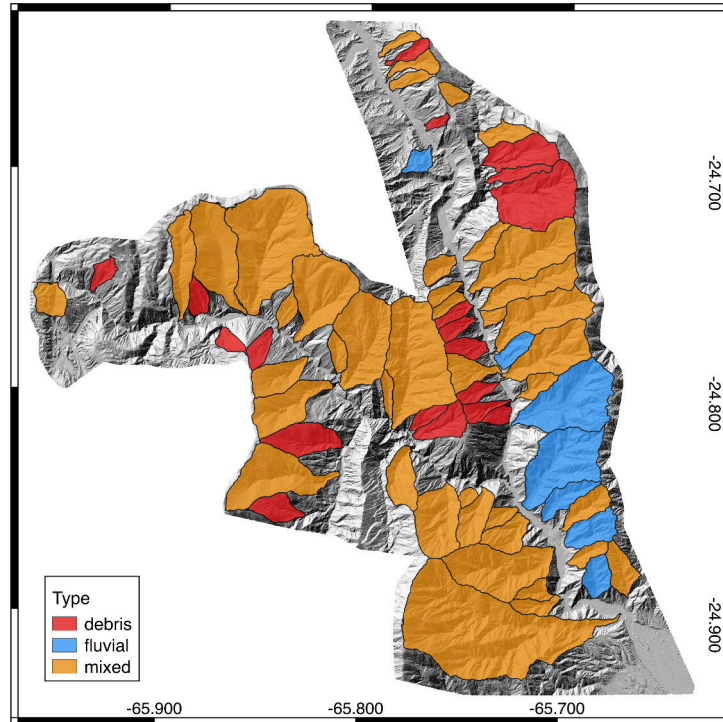


Figure 4.4.: Hand-classified control catchments within the extent of the 3 m stereo DEM.

4.2.2. Automated debris-flow detection

The distinctive topographic signature of debris flows serves as a basis for identifying regions that have experienced slope movements. As I recognize localized variations of the $\log S \log A$ relation within the QdT, I aim to develop a detection method that incorporates these spatial disparities. As an initial approach, a linear regression, weighted by the number of values per logbin, is fit to the data. Applying a weight function mitigates the effect of scattering in high drainage-area logbins related to the lower number of samples in these areas. The slope (θ) of this linear model is significantly lower (steeper) for fluvial catchments compared to debris-flow dominated areas (Figure 4.5 A) and thus found to be a good criterion to distinguish between these two classes. A threshold is set at the intersection of both density functions at $\theta = -0.089$. Mixed basins show θ -values lying mostly in between the ones of fluvial and debris-flow dominated regions. However, there is too much overlap with the other two classes to make a clear distinction based on the slope of the initial linear model fit alone.

A single linear regression is a poor fit for the curved $\log S \log A$ relationship. There-

4. Methods

fore, I test if mixed catchments could potentially be differentiated based on the goodness of fit. As shown in Figure 4.5 B, Adjusted R^2 values are indeed higher for fluvial than for mixed basins, yet the lowest coefficients of determination are found in debris-flow dominated catchments. This detail is attributable to the fact that debris-flow basins are generally smaller than fluvial or mixed catchments. A smaller catchment size leads to a lower number of slope values per logbin and, consequently, higher scatter, especially at large drainage areas. Using R^2 as a classification criterion is therefore ruled out.

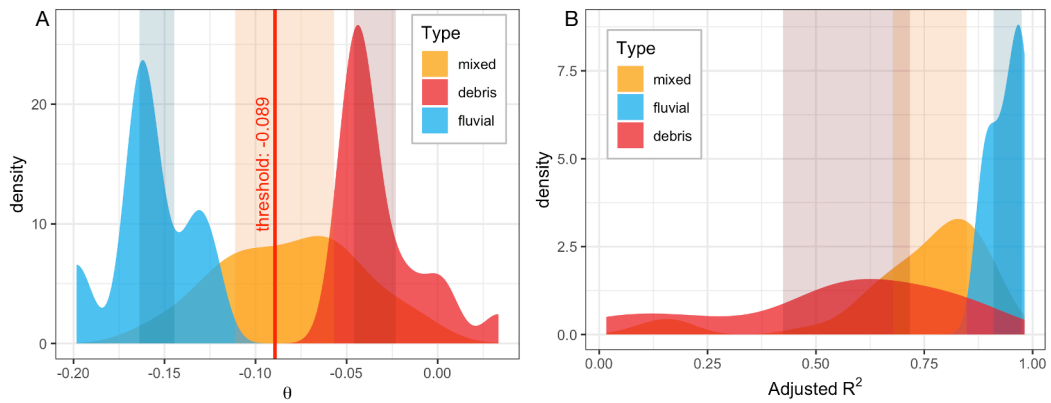


Figure 4.5.: θ -values of the initial linear fit separated by basin type with threshold employed in basin classification (A) and adjusted R^2 values of the initial linear fit to $\log S$ against $\log A$. Shaded areas indicate IQR.

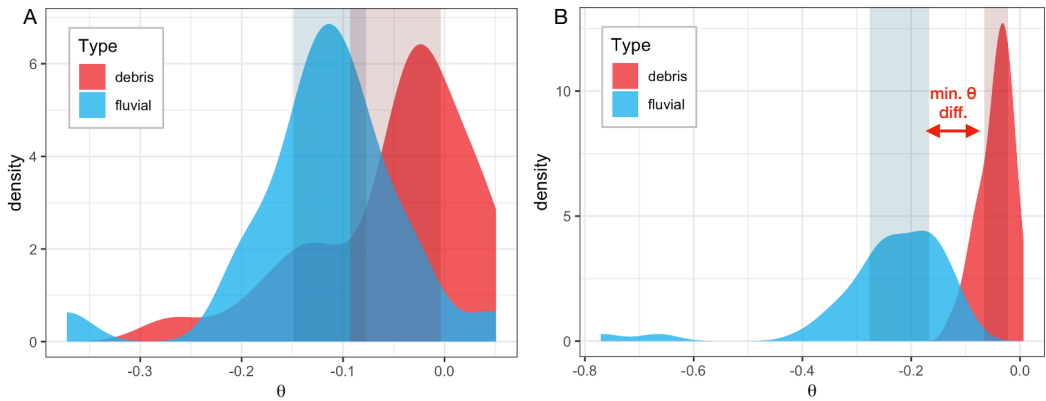


Figure 4.6.: Difference in θ values of first (debris flow) and second (fluvial) slope segments fitted to the $\log S$ $\log A$ relation for basins classified as debris flow or fluvially dominated (A) and mixed basins (B). Shaded areas indicate IQR.

4. Methods

Since most of the catchments in the QdT are of mixed type, I move away from initiating a classification through fitting just one regression line to the $\log S \log A$ relation. Mixed catchments are better described by a piecemeal linear relationship with one segment for the debris flow and one for the fluvial dominated part. These segments are determined through breakpoint analysis using the freely available segmented package (Muggeo et al., 2008) in R (<http://www.r-project.org>), assuming there is just one breakpoint marking the transition zone between debris flow and fluvial incision. A piecemeal linear model with a linear predictor is iteratively fit to the data until attaining the minimum residual standard error (Muggeo, 2003). As a first step, this breakpoint analysis is carried out for every single basin. Then, the individual regression line segments are investigated. As I enforce breakpoint detection on all catchment types, even those who do not show a noticeable kink, I expect the difference in slope (θ) between the two linear segments to be higher for mixed catchments than for those that are shaped by only one prevailing geomorphic process. Figure 4.6 highlights that there is indeed a pronounced θ -difference for mixed basins, compared to basins classified as debris flow or fluvially dominated. This inherent trait of mixed basins is utilized for basin classification. I take the difference between the 25th percentile of the first segment and 75th percentile of second segment slopes, which is -0.101, as a minimum threshold for a basin to be classified to be of mixed type. When overcoming this threshold, two linear segments are fitted to the data, and the breakpoint is estimated. Else, I assume that a single linear model is a good fit for the $\log S \log A$ relationship, and categorize the catchment according to the θ threshold dividing debris flow and fluvial basins (see Figure 4.5 A). A schematical representation of the final classification process is depicted in Figure 4.7.

The outcome of this automatic classification approach is evaluated against the manual classification for all 68 control catchments (Figure 4.8 A, Figure 4.9 A). Auto-classification scored an accuracy of 85.28 % and is thus found to be useful for basin classification. Deviations from the manually assigned classes attribute exclusively to breakpoints that were found by the algorithm and not detected by eye and vice versa. Most importantly, however, there were no mismatches between the two endmember classes, *debris* and *fluvial*.

4.2.3. From catchments to squares

An issue related to debris-flow dominated catchments is, as previously stated, that they are often much smaller than river basins. Capturing all debris-flow dominated catchments is not feasible through setting a minimum threshold of one square kilome-

4. Methods

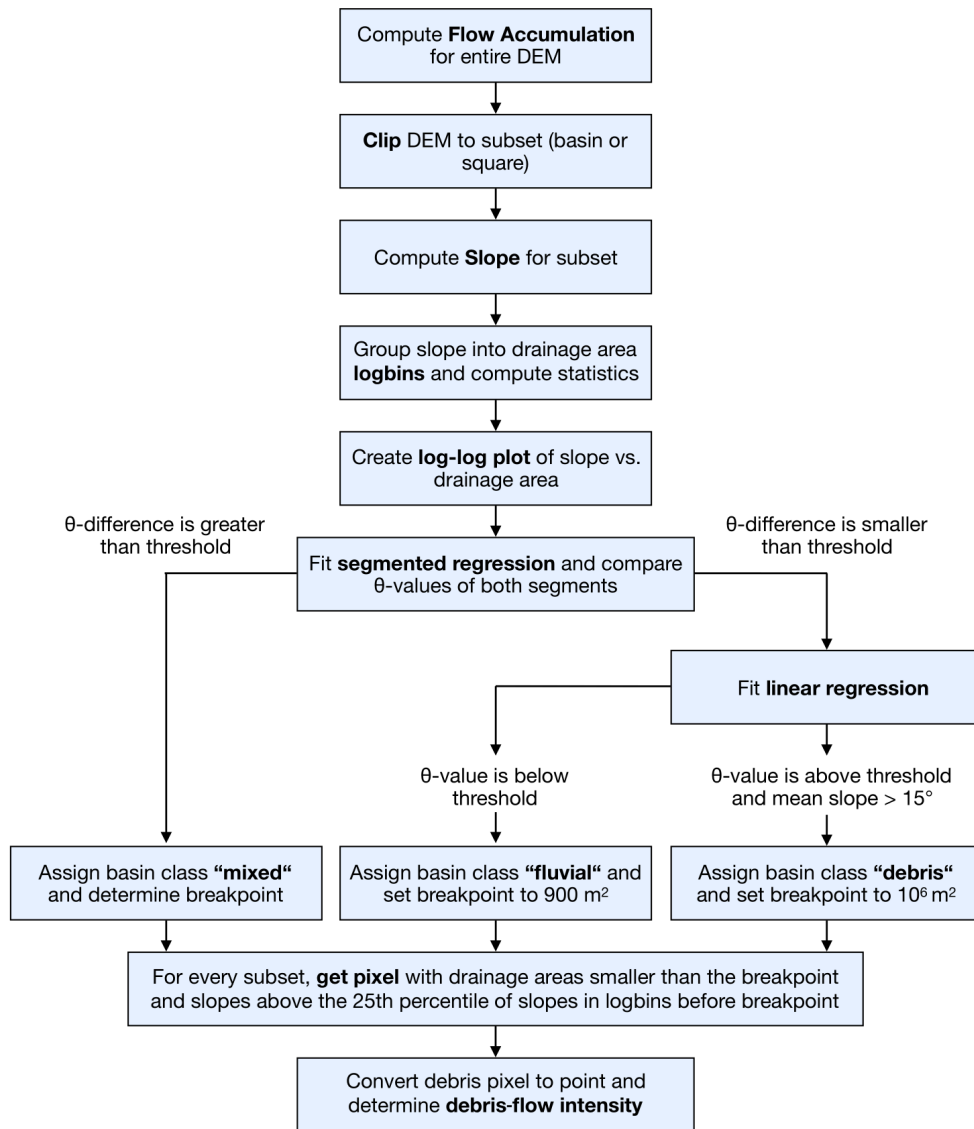


Figure 4.7.: Schematic overview of the steps involved in the automatic debris-flow detection.

ter for basin size. Nevertheless, these regions need to be included in the analysis to get a faithful debris-flow hazard assessment. Lowering the catchment area threshold is not an option as this would increase scatter and complicate correct basin classification. Also, even with smaller sized catchments, not all areas of the QdT would be investigated. My aim, however, is to use all of the high-resolution topographic data available to produce a continuous debris flow map for the lower part of the Río Toro catchment considering local variabilities. For this reason, I abstain from

4. Methods

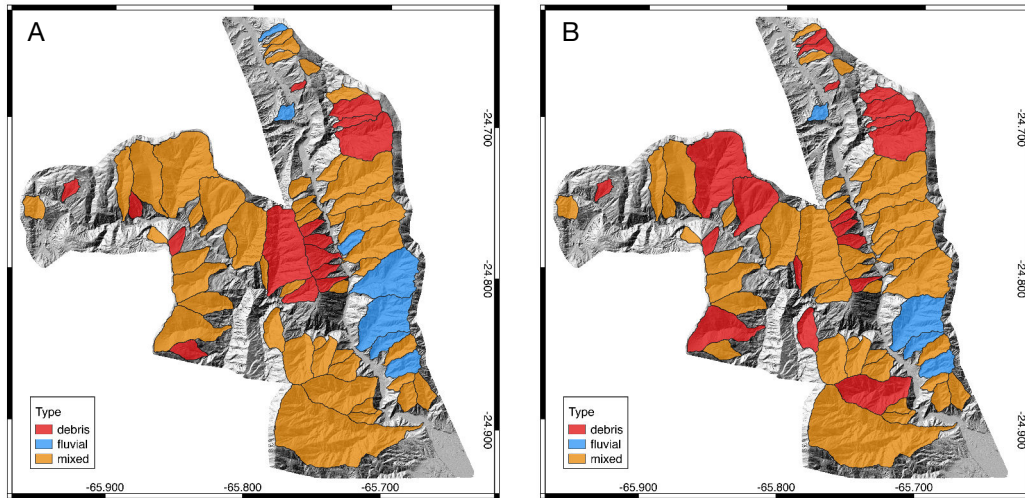


Figure 4.8.: Auto-classified test basins with topographic information and thresholds from 3 m stereo DEM (A) and TanDEM-X (B).

limiting the debris flow analysis to individual basins, but tile the study area into equally sized adjacent squares instead. The size of these tiles must be large enough to cover different parts of a watershed to avoid, e.g., hilltop effects, yet small enough to depict local geomorphologic variations. For the QdT, I work a square size of 4 square kilometers, which has been found to be optimal in terms of coverage and noise. In other regions of the world, this parameter may need adjustment depending on the local conditions.

The drainage area can no longer be computed separately for each square when moving away from closed drainage basins. Thus, the overall flow accumulation is investigated beforehand and then tiled to get accurate measurements of the drainage area. I further realize that some basins are cut-off, especially in the NNW part of the high-resolution DEM. For this reason, I complement the 3 m stereo DEM with TanDEM-X, resampled to match the resolution, and compute the flow accumulation for the entire Río Toro watershed.

4.2.4. Debris-flow detection on TanDEM-X data

To assess debris-flow hazard at a greater scope, I explore to which extent lower resolution topographic data are applicable for debris-flow detection via their topographic signature. Figure 4.10 shows the $\log S$ $\log A$ relation for the same test catchments illustrated in Figure 4.3 with slope and drainage area extracted from TanDEM-X and

4. Methods

A	<i>debris</i>	<i>fluvial</i>	<i>mixed</i>	B	<i>debris</i>	<i>fluvial</i>	<i>mixed</i>
<i>debris</i>	13	0	6	<i>debris</i>	11	0	8
<i>fluvial</i>	0	6	1	<i>fluvial</i>	0	4	3
<i>mixed</i>	2	1	39	<i>mixed</i>	8	0	34

Figure 4.9.: Confusion matrices comparing results of manual classification with auto classification using topographic information and thresholds from 3 m stereo DEM (A) and TanDEM-X (B). Columns represent the manual assigned classes from the reference data set, rows indicate the automatically assigned classes.

SRTM. It is immediately noticeable that TanDEM-X and, in particular, the SRTM DEM show significantly higher scatter as there are fewer pixels available in each logbin. A distinction between debris flow and fluvial processes at small drainage areas, where debris flows mostly occur, seems not feasible for 30 m SRTM data, because there is too much overlap between the two classes. The TanDEM-X DEM with a resolution of 12 m, however, offers a clearer distinction in θ values for debris flow and fluvial dominated parts. Therefore, it can potentially provide reasonable results when applying the classification method proposed for high-resolution data.

When working with a different dataset, the thresholds employed in the classification algorithm need to be adjusted in the same way as for the 3 m stereo DEM (Figure 4.11). With a value of -0.099, the θ threshold for distinguishing between debris flow and fluvial catchments is slightly lower. Also, the minimum θ difference to be overcome is smaller, possibly leading to more basins being classified as *mixed*. Again, the performance of the classification algorithm is evaluated against manual classification, scoring accuracy of 72.06 % (Figure 4.8 B, Figure 4.9 B). When interpreting this value, however, one needs to consider that the initial hand classification might have been different when using the $\log S \log A$ relation derived from 12 m TanDEM-X data as a basis.

To obtain an overview of debris-flow activity in the entire Río Toro catchment, the catchment extent is gridded into squares covering 4 square kilometers. Detection of debris-flow signature and the computation of debris-flow intensity are carried out in the same way as for the 3 m stereo DEM. I abstain from setting a lower drainage area threshold of 100 x pixel size and keep 900 m^2 as a lower limit since a threshold

4. Methods

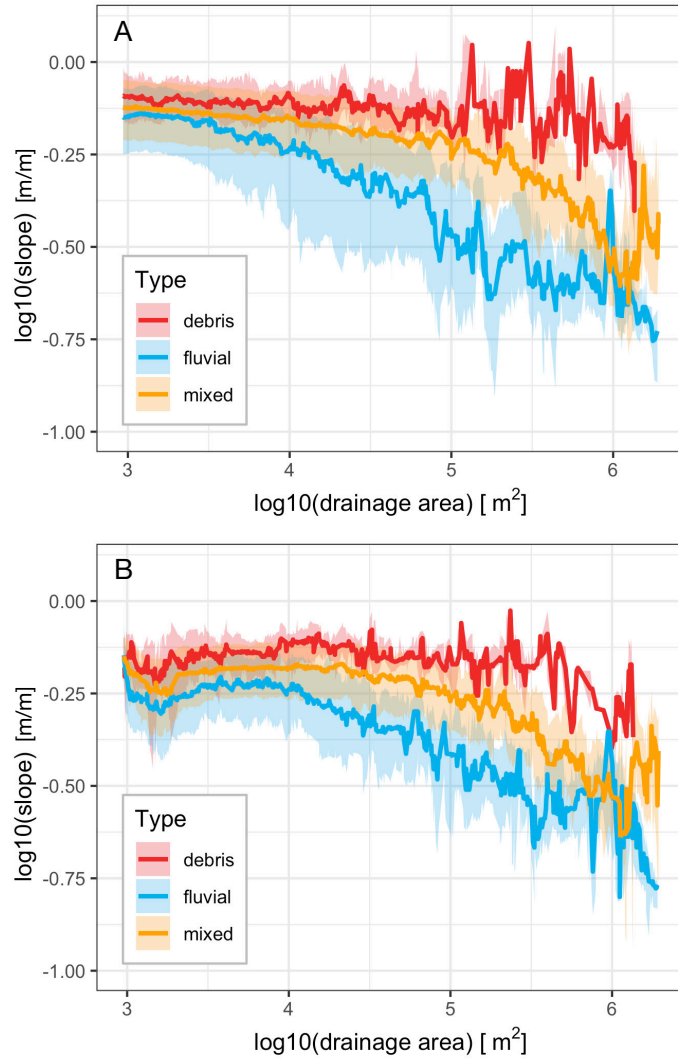


Figure 4.10.: Relation between topographic slope and drainage area in log-log space for three exemplary control basins with values extracted from 12 m TanDEM-X (A) and 30 m SRTM (B).

of 14400 m^2 would neglect too much data at low drainage area and aggravate reliable piecewise regression fitting.

A final adjustment is made to the classification algorithm as it fails to correctly interpret regions that are covered by vast, low-sloping alluvial fan and river-terrace deposits in the upper reaches of the Río Toro catchment. These regions typically exhibit no great change in slope with increasing drainage area. Therefore, the fitted regression has a θ value that is very similar to debris-flow dominated catchments, and the area is wrongly classified to be of *debris* Type with a breakpoint equal

4. Methods

to one square kilometer drainage area (see Figure 4.12). The occurrence of debris flows on such low gradient terrains is, however, implausible. Debris flows typically initiate on slopes greater 15° or 26.8 % (Takahashi, 1981). With no steep slopes around, it is improbable that any debris flows will affect these areas. To characterize cells that exclusively cover river terrace deposits, I introduce a third threshold equal to 26.8 % slope. If a basin or square exhibits a topographic signature supposedly matching debris flow deposits, the overall slope of the basin is investigated. If the mean slope of the investigated area is below 26.8 %, it will be attributed to a fourth class: *unclassified*.

4.2.5. Computing debris-flow intensity

The shape of the $\log S \log A$ relationship provides an estimate of the dominating incision process in the respective basin or square tile. Yet, it offers little information on how many debris flows exist in the region examined. Individual sectors exhibiting a characteristic debris-flow signature can, however, be identified by using the information obtained from breakpoint analysis. Following the assumption that the first segment of the piecewise linear model represents the debris-flow dominated part of a catchment, all pixels with a drainage area less or equal to the breakpoint are filtered. Secondly, a slope threshold corresponding to the 25th percentile of all slope values before the breakpoint or 15% is applied. I work with the 25th percentile rather than with the minimum of all slope values to avoid outliers. The remaining pixels are classified as debris flows. The intensity of debris flows is given by the number of debris-flow pixels per unit area, which is one square kilometer in my case. This measure allows the detection of areas that have experienced significant slope movement in the past and might likely show further debris-flow activity in the future. I also compute a kernel-smoothed intensity function of debris flows for visualization purposes using the *spatstat* library for R (Baddeley et al., 2004).

When working with TanDEM-X data, I realize that significantly more pixels, entire hillslopes even, are classified as regions of debris flow, causing a saturation of debris-flow intensity. This is attributed to the fact that the lower drainage-area limit of 900 m^2 is reached much faster at a pixel resolution of $12 \times 12 \text{ m}$ compared to the 3 m stereo DEM. To stay comparable between the two different datasets and only investigate channelized areas, the drainage area threshold is elevated to 7200 m^2 for TanDEM-X, which is equal to $50 \times$ pixel size. I pick this number as the outcome is proportionate to the results of high-resolution data. A threshold of $100 \times$ pixel size is unsuitable as the number of rejected pixels becomes large.

4. Methods

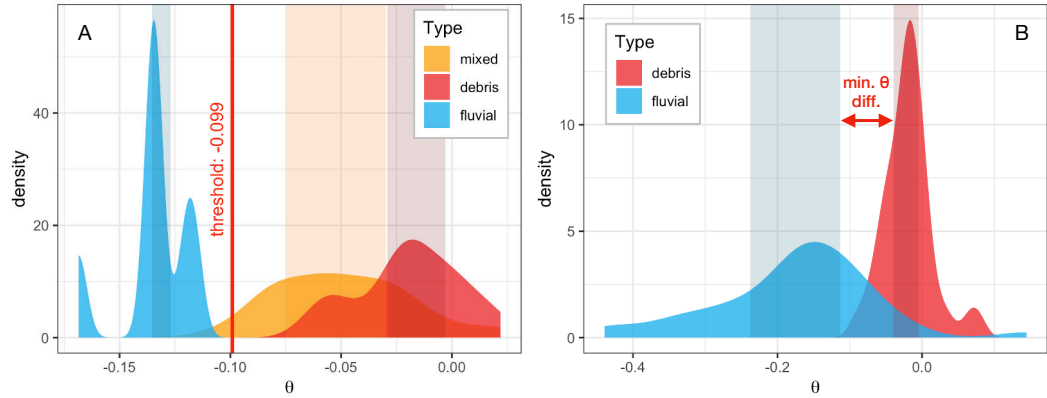


Figure 4.11.: θ thresholds for basin classification based on TanDEM-X data. Difference between θ of a single fitted regression line (A) and θ values for first and second slope segments of mixed basins (B). Shaded areas indicate IQR.

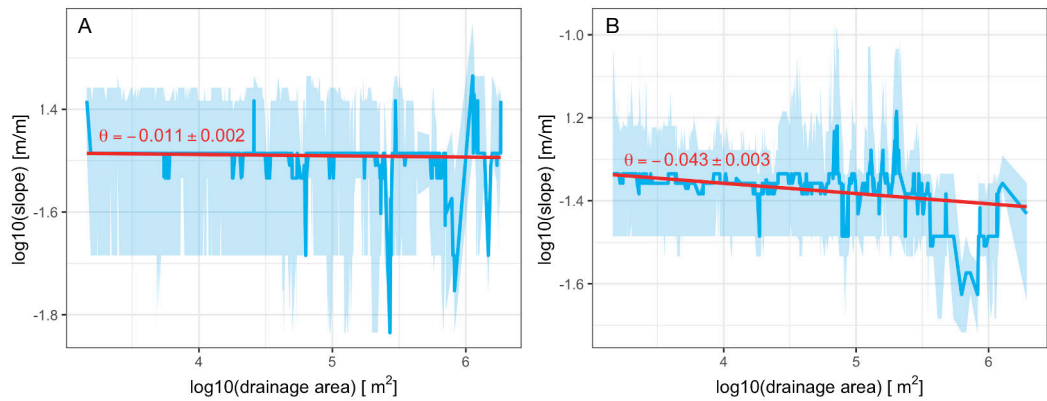


Figure 4.12.: Topographic signature and θ values of two exemplary squares covering low-sloping alluvial-fan deposits in the upper reaches of the Rio Toro catchment.

5. Results

5.1. DEM quality

Through testing various parameters involved in the different steps of DEM generation from stereo data described in section 4.1, I continuously determine the adjustments necessary for creating optimal high-resolution surface models in high-relief mountainous regions like the QdT using SPOT-7 data. DEMs created from stereo correlation of Cartosat-1 data are clearly inferior in quality to the SPOT-7 DEMs and are therefore only considered in more detail in the appendix (A.3). The assessment of DEM quality is carried through both visually and through differencing heights from triangulation to my ground-control data. For comparison with the dGPS measurements, I only use points for validation that did not find application during the DEM alignment. Heights from the DEM are extracted at the point locations with a buffer of 3 m.

One of the key findings, also emphasized by Beyer et al. (2018), is that considerable pre-processing of the raw data product significantly improves the stereo correlation outcome. Map-projecting imagery onto a pre-existing smooth DEM, in particular, enhances DEM quality. The existent DEM needs to be, however, selected with great care, as problems in the reference DEM directly translate to the final data product. The TanDEM-X DEM, for example, has immense problems in high-relief regions, which affects stereo correlation when stereo images are projected onto these erroneous regions (Figure 5.1 A + B). Creating a low-resolution reference DEM from the stereo data itself, as suggested by Beyer et al. (2018), is also ruled out as the triangulated surface does not show much relief, yet many holes and is very far away from the actual topography. Projecting imagery on such a surface produces a very noisy DEM (see Figure 5.1 C). The 90 m void-filled SRTM DEM brings about the best results when used in map-projection (Jarvis et al., 2008) (Figure 5.1 D). The void filled SRTM DEM is available for the entire Earth and might thus also serve as a reliable basis for stereogrammetric applications in other regions of the globe.

The impact of bundle-adjusting images before stereo correlation is not as pronounced. Also, contrary to my expectations, the use of ground-control points within the bundle

5. Results

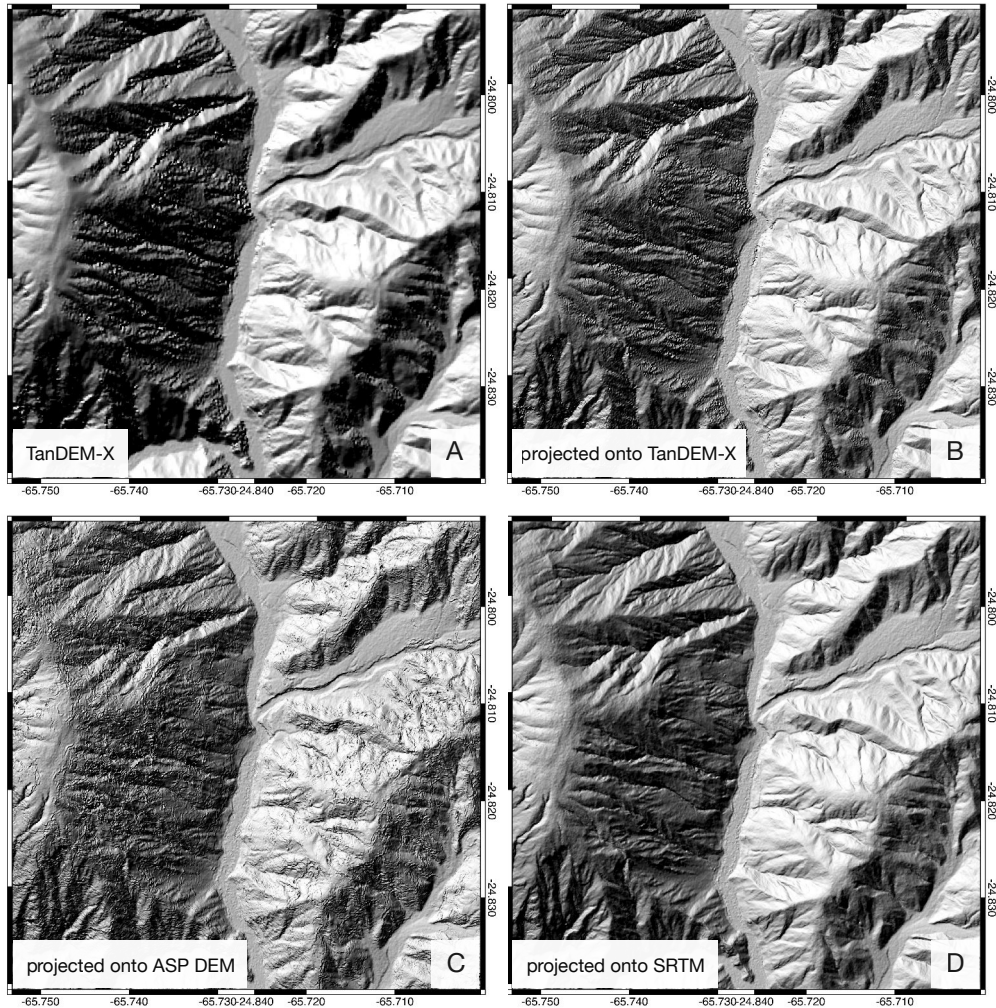


Figure 5.1.: Comparison of original TanDEM-X DEM (A) to stereo DEM map-projected onto TanDEM-X (B), stereo DEM map-projected onto low-resolution DEM created with ASP (C) and stereo DEM map-projected onto 90 m SRTM (D).

adjustment process does not seem to improve the accuracy of the final DEM in my case. Instead, it even increases the difference of the 3D surface to the kinematic ground control compared to bundle adjustment without ground-control points, as illustrated in Figure 5.2 A. In addition, the triangulated DEM displays offset from the static ground-control points that initially went into the bundle adjustment algorithm. The reason for this behavior is still unclear. The ground-control points were triple-checked in order to rule out familiar sources of error, e.g., a mix-up of longitude and latitude or wrong assignment of pixel coordinates. The residuals of all ground-control points

5. Results

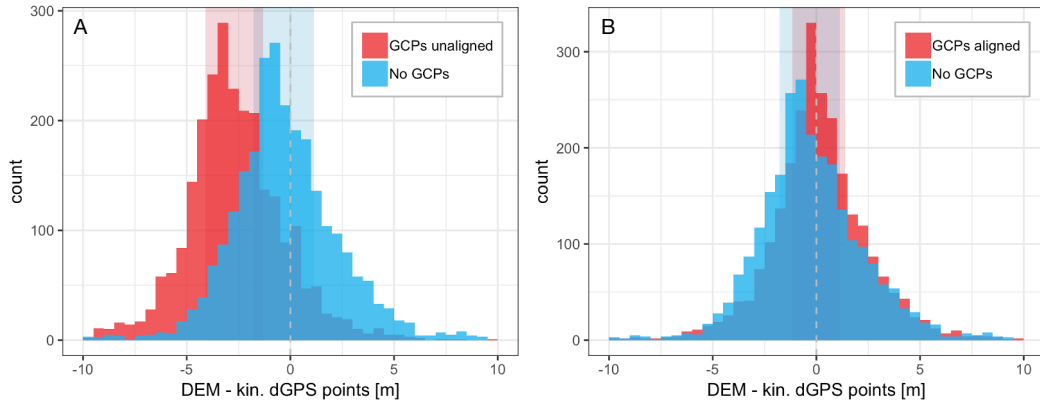


Figure 5.2.: Difference of stereo DEMs to kinematic dGPS points, comparing initial results of bundle adjustment with and without GCPs (A) and the aligned DEM, bundle adjusted with GCPs vs. a DEM created without any ground control (B). Shaded areas indicate IQR.

are furthermore well below 1 pixel, attesting to the assumption that no incorrect input of the ground-control data is causing the offset. I further tried to reduce the camera weight, which keeps camera positions and orientations close to their original values, to put more emphasis on the ground-control points during the bundle-adjustment process. However, this resulted in an even further aberration from the validation points. I suspect that the offset could arise from differential heights of the reference DEM used for map-projection. Comparison with my ground-control data show that heights from both SRTM and TanDEM-X differ significantly from the z-values I measured in situ. This discrepancy might have slightly affected the elevation of my final data product, especially since the DEM produced through map-projection onto a low-resolution DEM created with ASP itself aligned well with the ground control (see Figure A.4 C). Overall, however, it is to say that 23 ground-control points are likely not enough for a study area of several hundred square kilometers in size, especially not if they are all located more or less along a single axis. Ground control picking is generally error-prone, and thus, aligning the DEM to a significantly larger ground-control data set after stereo correlation seems like a more robust method to ensure spatial coherence of the final product (Figure 5.2 B).

Stereo correlation allows the adjustment of several processing parameters. The subpixel-mode determines the subpixel-refinement method. There are 12 different approaches to subpixel refinement implemented in ASP, most of which are, however, experimental or do not apply when using the default block-matching algorithm during stereo correlation (Beyer et al., 2018). In accordance with Beyer et al. (2018), I find

5. Results

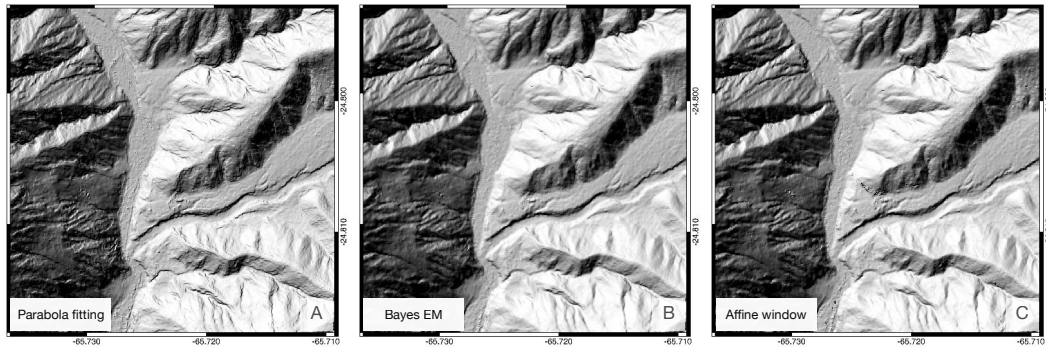


Figure 5.3.: Comparing the results of DEMs that were created using parabola fitting (A), an affine adaptive window with Bayes EM weighting (B) and an affine window only (C) during subpixel refinement.

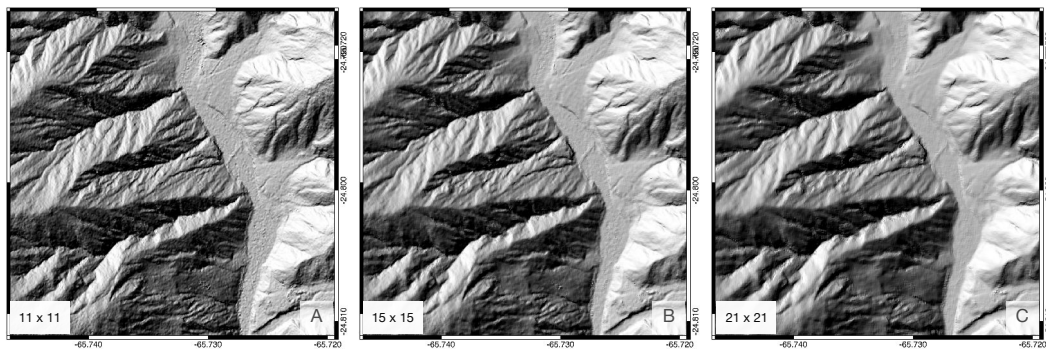


Figure 5.4.: Visual assesment of DEMs created with different kernel sizes during the stereo-correlation process. 11 x 11 pixel (A) 15 x 15 pixel (B) 21 x 21 pixel (C).

that the use of an affine adaptive window with Bayes expectation maximum weighting during subpixel refinement produces the best results, but takes more time (Figure 5.3). Nevertheless, a compromise in runtime usually implies a reduction in DEM quality.

The subpixel-kernel parameter sets the size of the correlation kernel in units of pixels. Keeping the kernel size slightly larger when using Bayes EM methods is beneficial, yet, smaller kernel sizes are better capable of depicting more complex high-relief features as present in the QdT (Beyer et al., 2018). Based on visual assessment, I favor a kernel size of 15 x 15 pixels, which seems to be a good compromise between surface smoothness and accurate representation of incision features (see Figure 5.4).

5.2. Debris-flow intensity derived from high-resolution DEMs

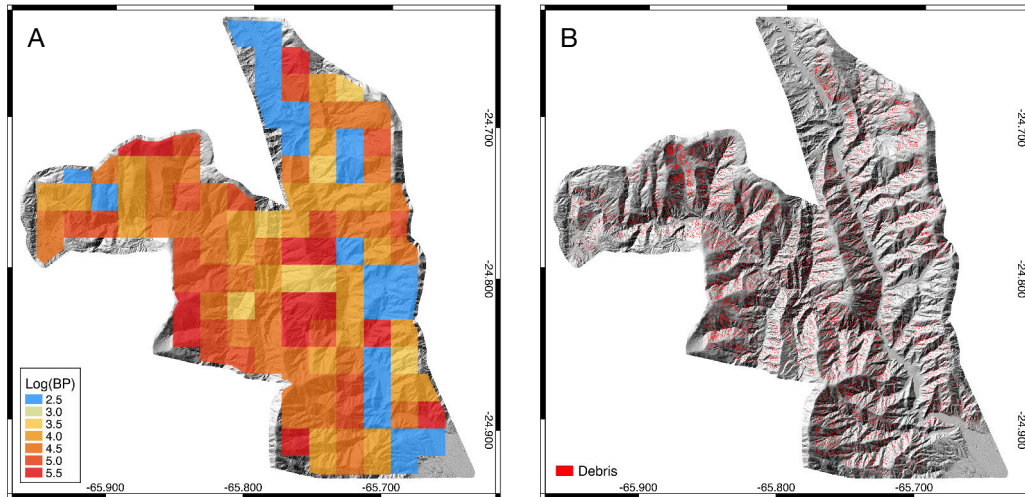


Figure 5.5.: Debris-flow identification for QdT using high-resolution topographic data. Tiles cover an extent of 4 km^2 and are colored by estimated breakpoint location (A). Extracted debris-flow pixels (B).

Results of the breakpoint analysis for squares covering the SPOT-7 aerial imagery are presented in Figure 5.5. Tiles which show topographic signature resembling fluvial test catchments are mostly located in the western part of the investigated area, covering the lower, more humid regions of the QdT to the south, but also extend to more arid reaches further north. Squares exclusively exhibiting a debris-flow signature are rare. Most regions show a break in the $\log S \log A$ relation at which breakpoints at high drainage areas are more common within the Río Capilla catchment. These results largely correspond to the manual classification of the test basins displayed in Figure 4.4. An inspection of the debris-flow intensity maps in Figure 5.6, it is clear that the areas of highest debris-flow-intensities do not entirely correspond with the cells classified as debris-flow dominated. Intensity, reflecting the number of debris-flow pixels within one square kilometer, has been normalized by the maximum intensity, to be able to compare between results from the stereo DEM and TanDEM-X data with different pixel size. The highest intensities are again found in the Capilla catchment, especially in one particular basin to the NW of the SPOT-7 data coverage. Regions that showed a clear indication of debris-flow activity during my field campaign in March 2019 showed only intermediate debris-flow intensities compared to on the

5. Results

slopes of the lower Río Capilla catchment. As this area is particularly hard to access, there is no field proof of this unusually high debris-flow activity. However, air photos suggest that these results are accurate (Figure 5.7). The slight discrepancy between assigned class and debris-flow quantity highlights the importance of translating the results of the topographic analysis back into 2D space, as the $\log S \log A$ distribution provides no information on how common particular slopes or drainage areas are within a specific area.

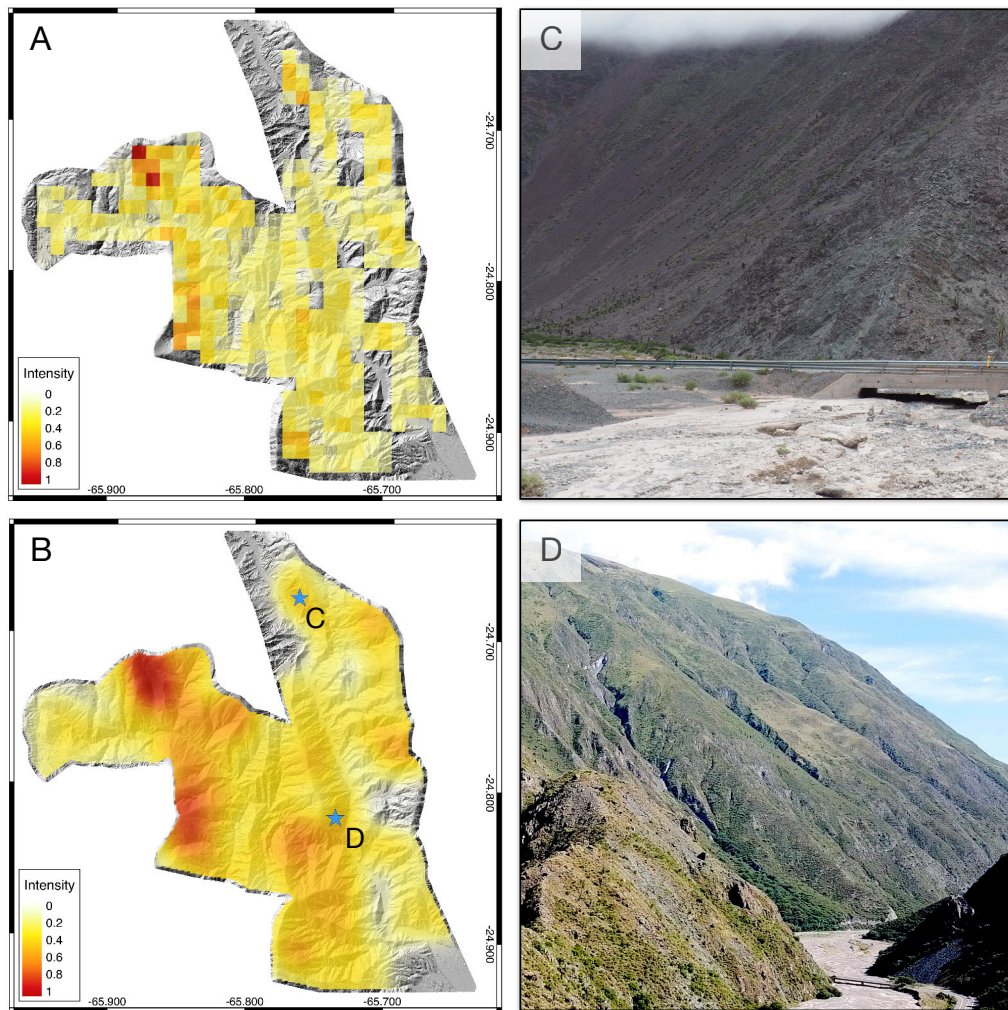


Figure 5.6.: Normalized debris-flow intensity determined through quadtrat counting (A) and normalized kernel-smoothed intensity function (B) for QdT based on high-resolution topographic data. Blue stars indicate regions that stood out as debris-flow prone during the field campaign, portrayed in (C) and (D).

5. Results

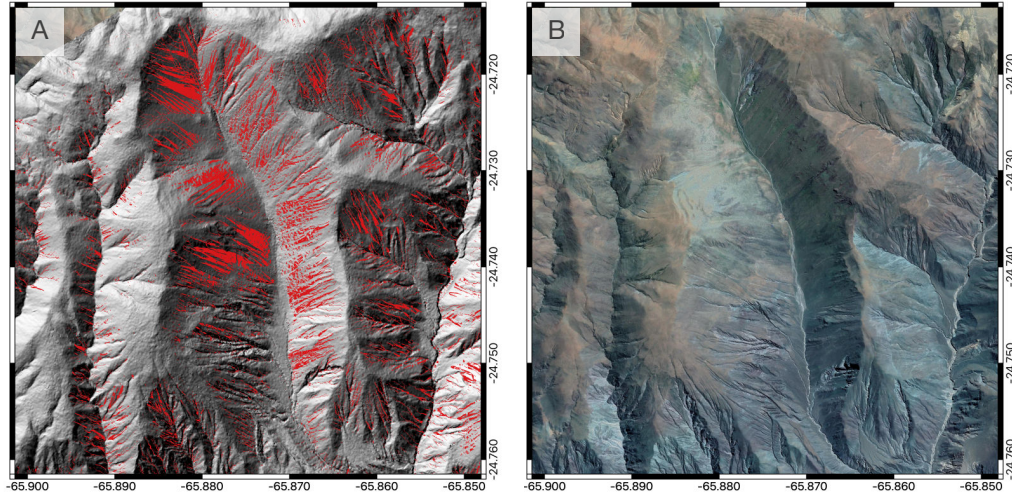


Figure 5.7.: Comparing estimated locations of debris flows (A) to satellite imagery from Google Maps (B).

5.3. Debris-flow intensity from TanDEM-X data

Extracting debris flows based on lower resolution TanDEM-X data slightly changes the resulting debris-flow intensity. Figure 5.8 shows that overall, higher intensities are more evenly distributed, which does, however, not mean that intensities are generally higher. Most areas highlighted in Figure 5.8 B also show high debris-flow intensity values in the 3 m data, yet, appear much less obtrusive in the face of the tremendously high intensities of a single catchment. In the TanDEM-X data, the highest intensities are no longer concentrated solely on the particular basin within the lower Río Toro catchment depicted in Figure 5.7 but have shifted to the southeastern flank of the Capilla basin. Regions that did show signs of recent debris-flow activities in the field are more noticeable due to higher intensities. The southeastern flank of the QdT appears entirely free of any debris flow, while a higher-resolution data set suggests slight debris-flow activity. Results of breakpoint detection based on the stereo and TanDEM-X data are similar to previous estimates based on high-resolution data, except for a few individual squares (Figure 5.9). Only three tiles received a completely differed classification of either debris or fluvial type, indicating a linear $\log S \log A$ relationship that is close to the θ thresholds distinguishing between the two endmember classes.

On a larger scale, I find that within the entire Río Toro catchment, higher debris-flow intensities go hand in hand with higher relief, and are particularly found within

5. Results

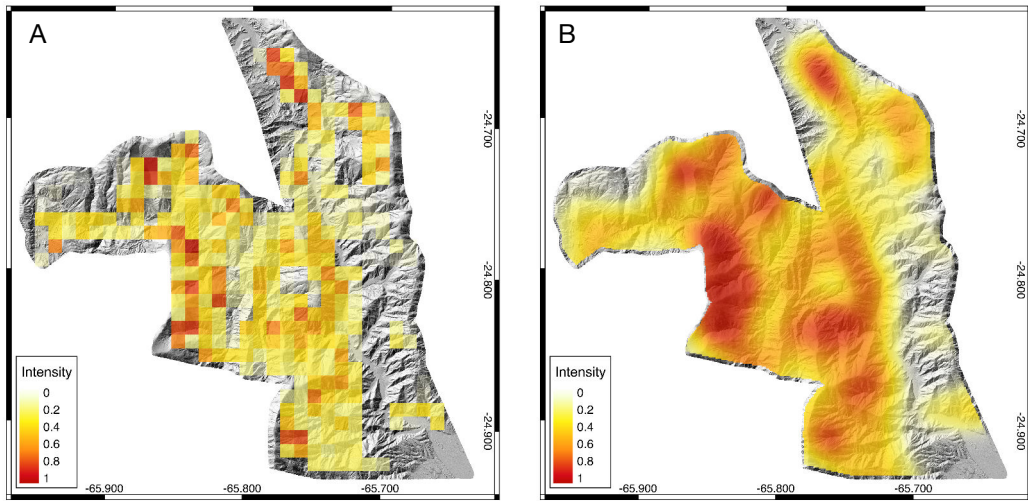


Figure 5.8.: Normalized debris-flow intensity determined through quadrat counting (A) and normalized kernel-smoothed intensity function (B) for QdT based on TanDEM-X data.

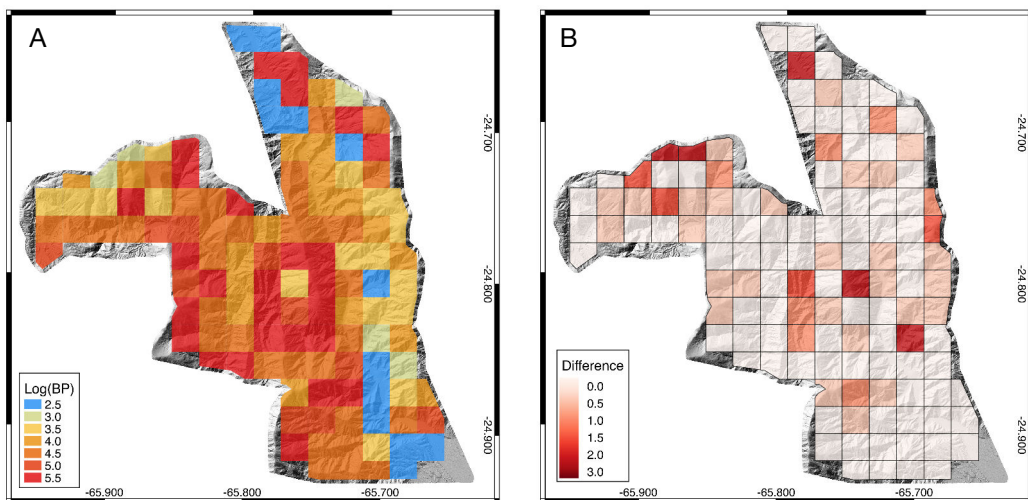


Figure 5.9.: Results of breakpoint analysis based on TanDEM-X data (A) and absolute difference of breakpoint location compared to results from stereo DEM (B).

the deeply entrenched gorge and on the Eastern flank of the drainage basin (Figure 5.11). Squares classified as *fluvial* dominate the low-sloping upper reaches of the Toro catchment, with interspersed by patches of areas exhibiting mixed topographic signatures (Figure 5.10 A). Regions purely expressing debris-flow signature are rare

5. Results

and again limited to greater topographic gradients. Looking at the location of the transition between debris flow and fluvial topographic signature in Figure 5.10 B, I find that it occurs at higher drainage areas throughout most of the southern part of the Toro catchment. In contrast, this transition is found in drainage areas that become smaller towards the southwest.

5. Results

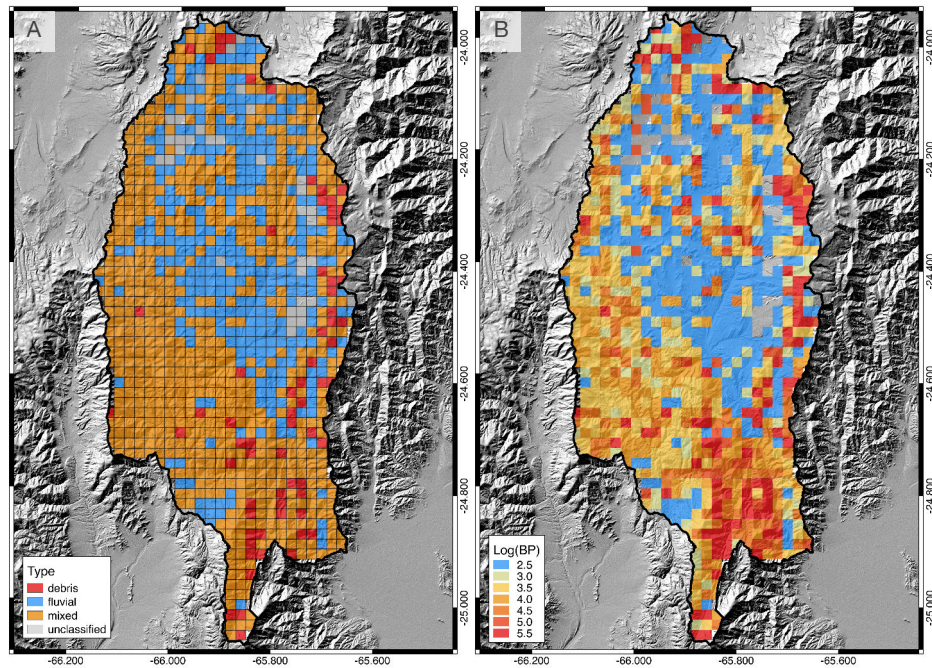


Figure 5.10.: Classifying of 2 x 2 km squares covering the entire Rio Toro catchment (A) and location of detected breakpoint (B).

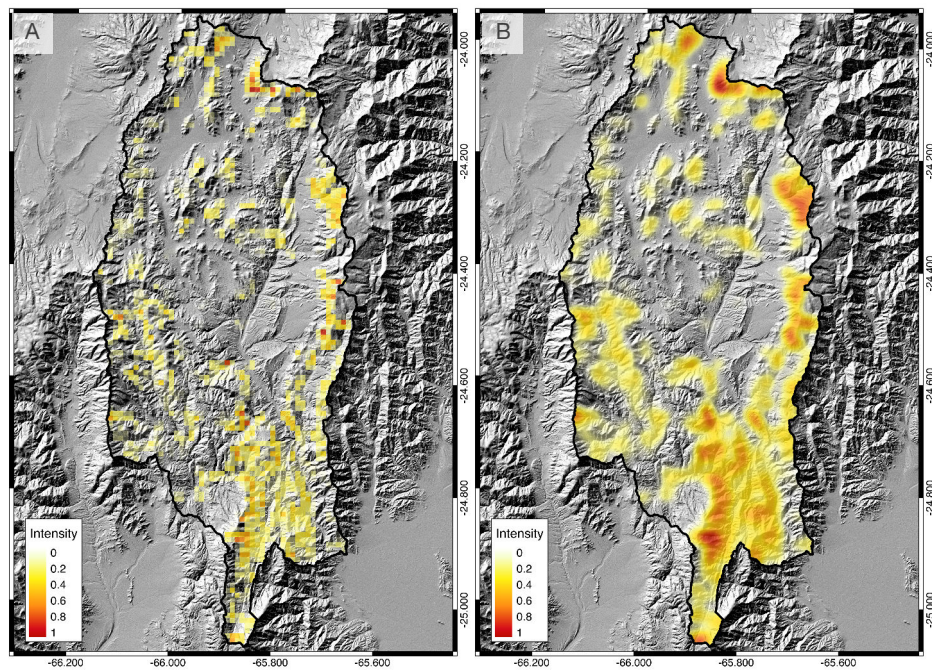


Figure 5.11.: Normalized debris-flow intensity determined through quadtrat counting (A) and normalized kernel-smoothed intensity function (B) for the entire Rio Toro watershed based on TanDEM-X data.

6. Discussion

6.1. Stereogrammetry as a tool for DEM generation

The great advantage of stereogrammetry is that it is a cost-efficient method to acquire high-resolution topographic information across large areas (Loghin et al., 2019). When based on aerial photography, obtaining good quality elevation models is, however, depending on local weather conditions. Imagery with severe cloud- or snow-cover is unusable as correlation will fail in obstructed areas. Aerial photography will further only picture Earth's surface cover, including buildings and vegetation. Thus, the resulting elevation data will only constitute a digital surface rather than a digital terrain model, implicating greater heights, rough surfaces, and elevated slope values (Nelson et al., 2009). Within the QdT, cloud coverage is a known issue in the lower part of the catchment. For this study, I was able to obtain a cloud-free scene. However, when working with several scenes from different acquisition dates, e.g., to analyze river bed aggradation, cloud obstruction might pose a more serious obstacle. As the lower reaches of the Toro catchment receive significantly more moisture than upstream areas, vegetation cover also plays a role in these sectors. Its presence certainly leads to a slightly higher surface in the South of my study area, and I cannot rule out that, e.g., the higher IQR of slopes in fluvial catchments is caused due to increased roughness from vegetation. For most parts, however, the QdT is relatively arid and only sparsely populated. In these regions, my DEM will reflect the bare Earth surface and is suitable for geomorphic analyses. Even higher than actual elevation values in the lower reaches of the catchment should not be of great concern as there is not much variation in canopy height. Consequently, the surface is uniformly elevated, which should not significantly affect the topographic signature. Overall, the surface model created from SPOT-7 stereo data shows significantly fewer errors, artifacts, or holes than comparable open-source products based on radar data. In high-relief regions, radar data are regularly impacted by topographic effects such as fore-shortening, layover, or shadowing because of the side-looking geometry of the sensor (Chen et al., 2018). In stereogrammetry, these effects decrease as objects are viewed from different angles – the more angles, the better. Hence, tri-stereo data

is the better choice when it comes to accurately depicting the topography of steep mountainous regions.

6.2. Potential of ground-control data

My results suggest that ground-control points have the potential to improve the accuracy of stereo DEMs. However, they are not mandatory in order to obtain good quality, internally consistent surface models. Optimally, ground-control points should cover the extent of the imagery evenly and include the corners. The main problem with acquiring ground-control data in the QdT is accessibility and also the potential to recognize a point on the satellite imagery. As 4.5 years separate the acquisition of the SPOT-7 scene and the field survey, I require eye-catching, perennial features, which are usually human-made structures such as bridges or road intersections. Within my study area, all infrastructure concentrates on the narrow gorge created by the Toro river. Consequently, all ground-control points lie on or in the vicinity of the main road in a north-south orientation. As there is not much lateral shift, the points create an axis along which the DEM tilts when ground control values are introduced (Figure 6.1 A). If this tilt is a better representation of the real surface elevation or not is debatable, as there is no suitable dataset for comparison. TanDEM-X data, for example, show a difference of up to 55 m to the stereo data (Figure 6.1 B).

Due to the spatial orientation of the ground-control data, their potential for assessing DEM quality also has its limitations. Low-relief regions with good contrast between the river, road, and rubble might be easier to correlate than steep slopes. For these, potentially error-prone regions, however, validation data is missing. Nevertheless, my control dataset did reveal that the use of ground-control points in the bundle adjustment process does affect the resulting DEM. While the GCP-adjusted DEM initially shows a greater offset to the validation points, the overall distribution of values is tighter than it is for the DEM adjusted without any ground control (Figure 5.2). Through point-cloud alignment, the triangulated height values correspond well with the ground-control data. In contrast, without ground truth, the final product might have a vertical offset of a couple of meters depending on the accuracy of the satellite meta-data and the reference surface used during map-projection. In this regard, ground-control data does increase spatial accuracy. Pinpointing a DEM to meter accuracy is, however, not necessary for most geomorphic analyses as internal consistency is the critical variable here. DEMs sufficiently suitable for these purposes can be obtained from remotely sensed data alone.

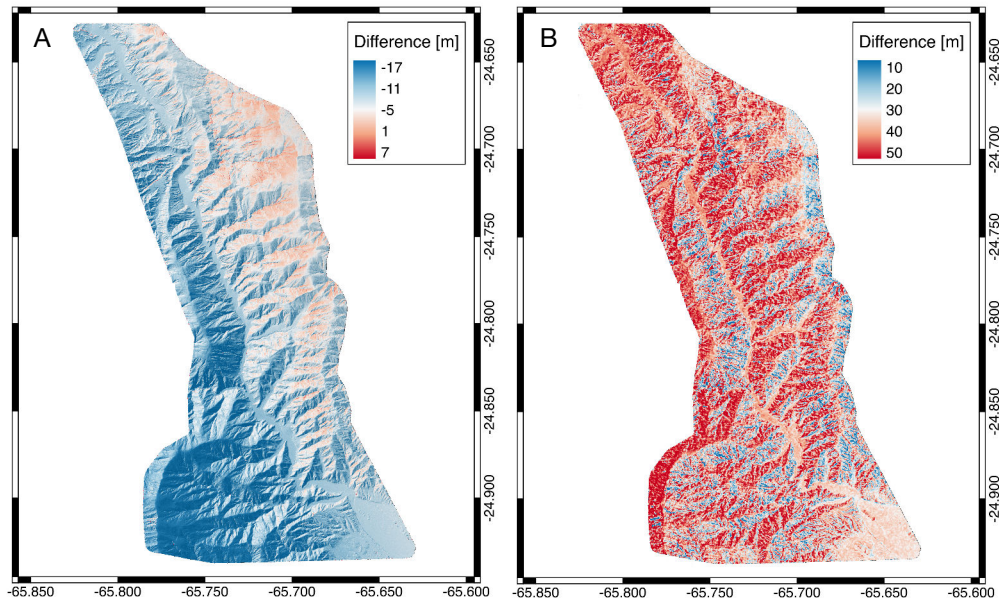


Figure 6.1.: DEM adjusted and aligned with ground control data differenced against a DEM created without any ground control (A) and TanDEM-X (B).

6.3. Challenges of debris-flow detection

My approach to detect debris flows is utterly new. It is entirely based on the specific topographic signature of debris flows constrained through intensive fieldwork by Stock and Dietrich (2003). Its design is relatively simple, easy to comprehend, and applicable to more extensive areas, as it relies on topographic information only. Therefore, it can be utilized for assessing debris flows in any region covered by a DEM of sufficient spatial resolution. Thresholds, limits, and kernel sizes for investigation can be adjusted accordingly. Simplicity is also a drawback – my method does not account for any preconditioning factors such as lithology, vegetation cover, or rainfall. Including these might, however, not be necessary because the result of sparse vegetation, loose material, and heavy rainfall is the debris flow itself, which will be recognized due to its unique $\log S \log A$ relation. Conversely, however, my results can be used to identify processes that promote debris flow, which will be discussed in the following section.

A great advantage of my approach is its ability to account for spatial variety of geomorphic processes, whose sensitivity can be adjusted through changing the size of the individual squares that will be analyzed. Using squares instead of closed

6. Discussion

basins is a necessary step to include small debris-flow catchments. This technique may cause averaging of topographic signatures from different basins. However, I do expect no dramatic change in dominating processes between two adjacent catchments. Therefore, the averaging effect is negligible as long as the size of squares does not cover vast regions.

High-quality input data is crucial for obtaining high-quality results. High-resolution stereo DEMs produce clear plots of slope against drainage area, which facilitates any automatic approach to basin classification. TanDEM-X data with a resolution of 12 m is the limit of what is reliably classifiable. Larger pixel sizes and errors in the DEM introduce significantly more scatter, which can obscure the topographic signature. Obvious misclassifications occurred in the northern part of the Toro catchment showing pronounced breakpoints on a very low-sloping terrain (Figure 5.10 B). These were not caught by the threshold introduced to avoid the misclassification of fluvial terraces as a breakpoint was estimated. Debris-flow intensity estimates are, however, not affected by these erroneously assigned classes, because the 15° slope threshold is reintroduced when extracting debris-flow pixels. Setting this threshold entails a slope dependency of the estimated locations of debris flows to some degree. Debris flows can cover large areas, including those below 15° . My approach, however, only identifies the initiation areas of debris flows that require a minimal topographic gradient. Generally, I noted that the chosen approach does not perform well in low-relief areas, but it is also not intended for these regions. In the steep-sloping southern part of the QdT, TanDEM-X data are compatible with the ones from higher-resolution equivalents. The differential class assignment here results from varying thresholds separating fluvial and debris-flow signatures. The established thresholds play a critical role in the results of basin classification. A robust set of control catchments covering the variability within the entire study area is indispensable.

6.4. Factors triggering debris-flow activity

Debris flows result from the interplay of several factors, including local relief, availability of unconsolidated sediment, climate, vegetation cover, and tectonic setting (e.g. Costa (1984)). As debris flows are gravity-induced mass movements aided by water, topographic relief is an important initiation factor of debris flows (Klubertanz et al., 2009). The relation between steep slopes and debris-flow abundance is well illustrated in Figure 5.8. Highest debris-flow intensities are associated with the steepest parts of the Toro catchment, namely the bedrock gorge and the eastern flank. Local relief is

6. Discussion

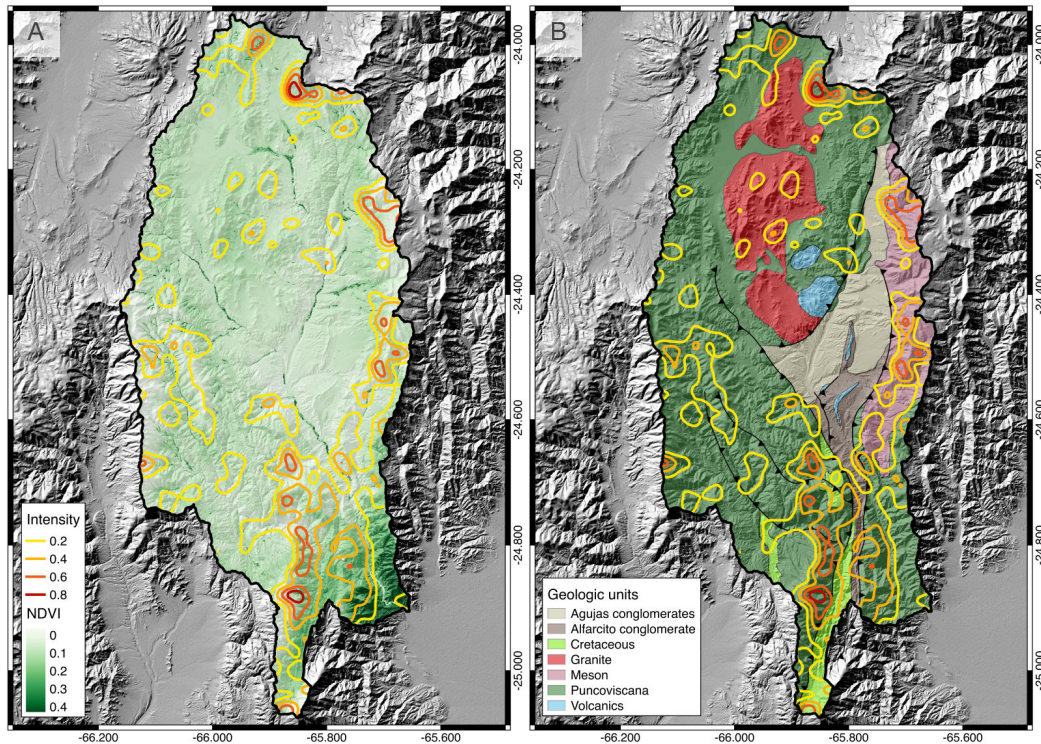


Figure 6.2.: Maximum NDVI mosaic from Landsat 8 scenes acquired in October 2014 (A) and geologic map of the Quebrada del Toro indicating lithologic units and main fault strands adapted from Tofelde et al. (2017) (B) together with debris-flow intensity contour lines.

undoubtedly a crucial factor for debris-flow initiation and mobility. In this section, however, I aim to explore preconditioning factors for debris flows that are not as evident.

To mobilize debris flows, a source of moisture is compulsory. However, the influence of water on slopes is variable. Water can destabilize fractured or unconsolidated rock through increasing pore pressure or gravity-driven groundwater-flow (Iverson and Reid, 1992). On the other hand, continuous water availability promotes the formation of soil and a thick vegetation cover that can enhance cohesion and strengthen slope stability (Collison and Anderson, 1996). Infrequent, extreme rainfall events are therefore considered to be a more effective driver of debris-flow activity than a constant source of moisture. Due to a lack of rainfall gauges stationed within the QdT that could provide data on intermittent rainstorms, I only investigate the effect of more sustained moisture using the normalized difference vegetation index (NDVI)

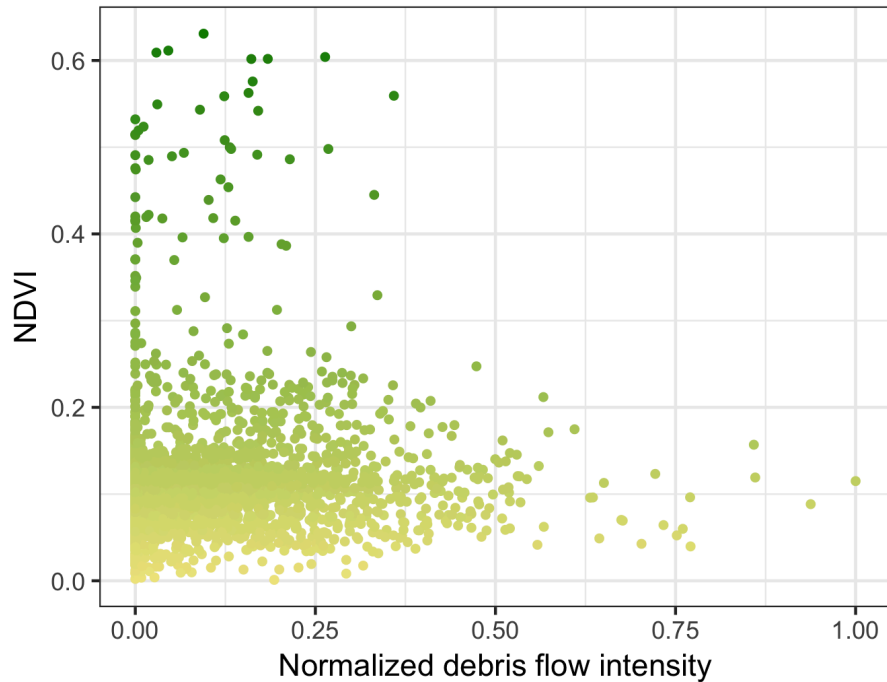


Figure 6.3.: Possible relation between debris-flow intensity and vegetation cover.

as a proxy for rainfall. NDVI values visualized in Figure 6.2 A result from a greenest pixel composite of eight Landsat 8 scenes acquired during October 2014 to match the acquisition time of the SPOT-7 data. To investigate the relationship between NDVI and debris-flow intensity, I extract and average raster values at equally spaced sample points with a distance of 1 km and a buffer of 500 m throughout the Río Toro catchment. The resulting relationship shows no clear trend (Figure 6.3). Nevertheless, the highest debris-flow intensities are exclusively found in regions with small NDVI values. In contrast, higher NDVI values generally imply less debris-flow pixels, which could hint at the stabilizing impact of vegetation coverage.

Another crucial factor for debris-flow activity is sediment supply. Individual debris flows are composed of material ranging from clay-sized grains to boulders (Iverson, 1997). These constituents must be available in order to supply mass to a slope movement. Strong, difficult to erode bedrock is therefore not the ideal substratum to feed a debris flow while weak, highly erosive rock might not be able to build a topography that provides sufficient gravitational potential energy. In the Toro basin, the most commonly exposed lithology is the metamorphic Puncoviscana formation. It consists of thick, pervasively sheared flysch units of late Proterozoic to early Cambrian age that are thrust over the conglomeric units in the northeast of the basin (Hilley

6. Discussion

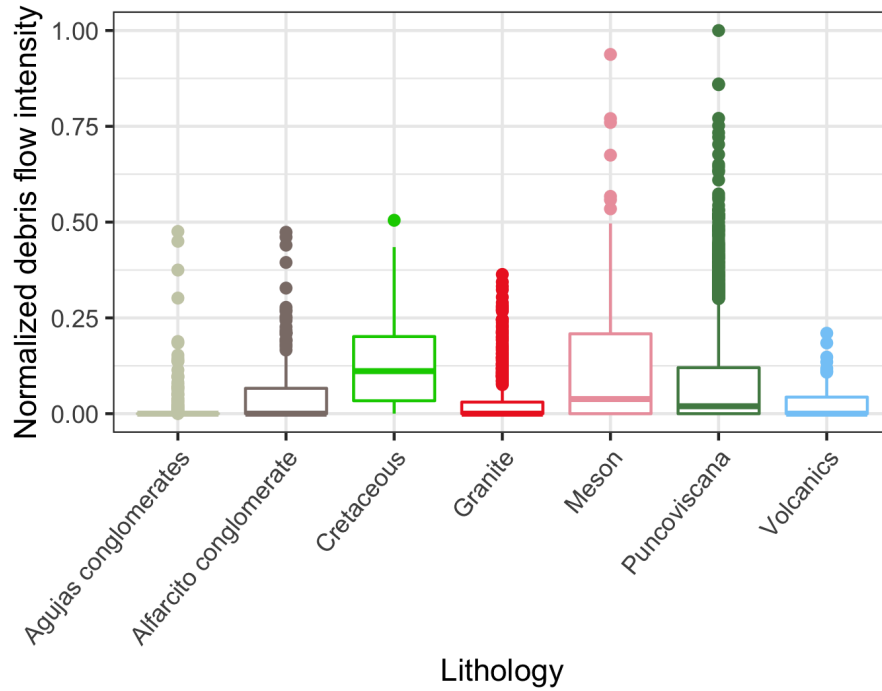


Figure 6.4.: Possible relation between debris-flow intensity and exposed rock type.

and Strecker (2005), Ježek et al. (1985)). This weakly metamorphosed material seems ideal for debris-flow generation as the active uplift and deformation of the Puncoviscana formation creates a significant topographic gradient (Hilley and Strecker (2005), García et al. (2019)). Additionally, the Puncoviscana's cataclacized character offers sufficient surface and incohesive material for weathering and erosion. Figure 6.4 shows that indeed the highest debris-flow intensity values are found within the Puncoviscana formation. This lithology does cover most of the Toro basin, including the shallow-sloping northern reaches. Hence, the 50th percentile of intensity values is lower for the Puncoviscana formation than for other lithologies. Apart from the Puncoviscana formation, only the Cretaceous units and the Mesón group indicate considerably higher debris-flow intensity values. Both are exposed in regions with pronounced relief. The Cretaceous sandstones of the Salta group crop out in the southern part of the Toro catchment, while the quartzitic Mesón group dominates the eastern flank, where faulting has produced significant rock uplift in the last 8.73–7.5 years (Hilley and Strecker, 2005). Due to their more resistant nature, both lithologies do not seem ideal to produce debris flow material. Nevertheless, the presence of steep slopes and ongoing faulting activity might outweigh the less suitable lithological conditions in these areas.

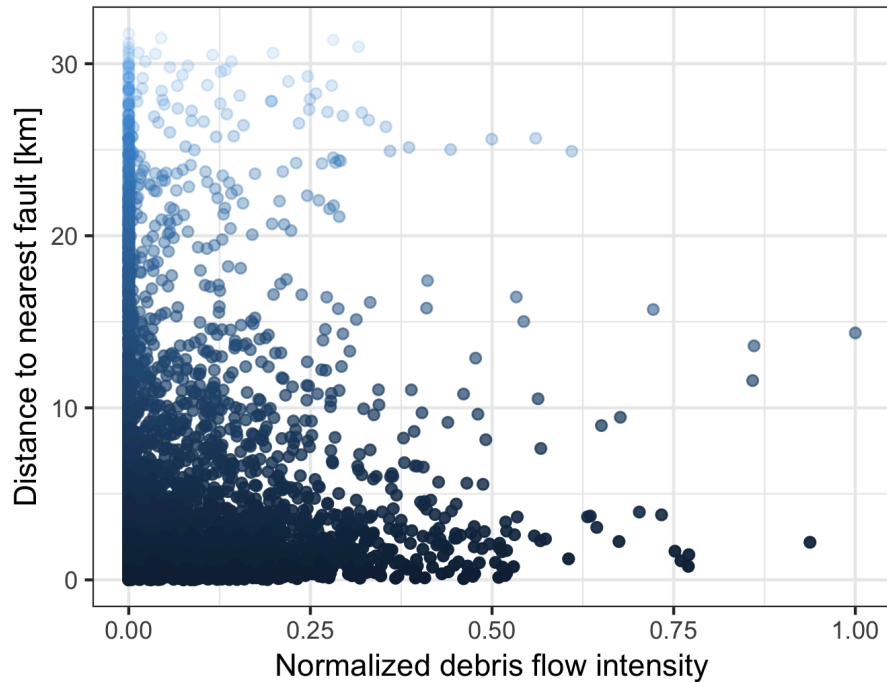


Figure 6.5.: Possible relation between debris-flow intensity and distance to nearest fault segment. Debris-flow intensities are extracted at equally spaced sample point locations that are then investigated concerning their distance to the closest fault segment.

Active faults are another factor to be taken into account when it comes to assessing debris-flow hazards. While deformational structures predispose regions to debris flows through the creation of topography, sudden rupture events can also trigger rock falls, and landslides that supply large volumes of unconsolidated material to subsequent debris flows (Tang et al., 2009). The QdT is dissected by several fault strands, including the west-dipping Solá Fault, the northwest-dipping San Bernardo Fault, and the east-dipping Gólgota Fault (Marrett and Strecker, 2000) (Figure 6.6). Principal deformation along the San Bernardo and Gólgota faults occurred before 0.98 Ma, while the Sólá fault segment is still actively deforming since the Pliocene (Marrett and Strecker, 2000). Hillslopes surrounding the Gólgota and Sólá fault show particularly high intensities of debris flows. Thrust-related topographic gradients most definitely promote debris-flow activity by enhancing gravitational pull. Therefore, higher debris-flow intensities are generally found in relative proximity to fault segments within the QdT (Figure 6.5). However, there are higher-relief areas that do not exhibit any topographic signatures of debris flows; these are the catchments along the south-eastern part of the QdT. These catchments have been

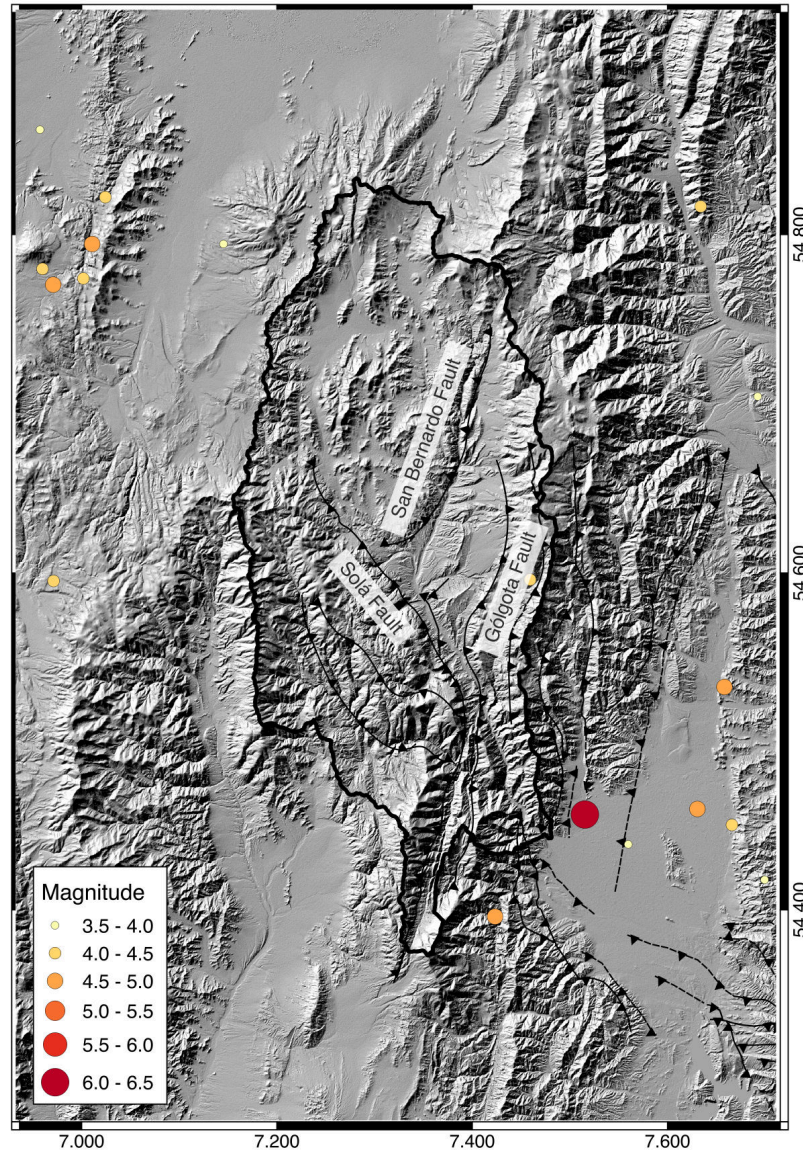


Figure 6.6.: Map of the main fault segments within the QdT and surroundings together with localities of all earthquakes with a magnitude > 2.5 that occurred between 2000 and 2020.

recognized to hold very low θ -values in the process of manually investigating the $\log A \log S$ relation (Figure 4.4). While they are situated in an area that does receive more moisture, they are also characterized by greater distances to the nearest fault segment. A possible interpretation is that rivers in these terrains had more time to undisturbedly cut this stable topography and establish the topographic signature of fluvial incision with higher rainfall rates supporting this process. A similar expla-

6. Discussion

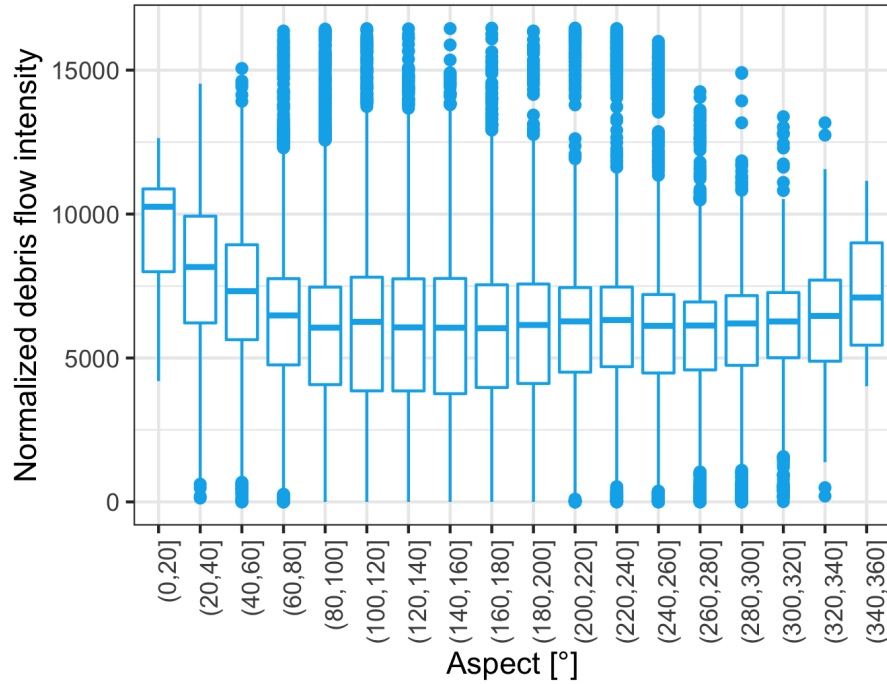


Figure 6.7.: Possible relation between debris-flow intensity and slope aspect.

nation could potentially apply to the San Bernardo fault to the north of the Toro catchment, which shows only minimal signs of debris-flow activity. Of the three main fault segments, the San Bernardo fault has been inactive for the longest time, since reactivation of the Gólgota fault after 0.98 Ma has been suggested by Hilley and Strecker (2005). Longer quiescence implies a longer time for fluvial incision to imprint its topographic signature and cut steep slopes that might previously be particularly vulnerable for debris scour. Furthermore, the San Bernardo fault traverses an area that is dominated by conglomerates, which are frequently re-transported in well developed river valleys. These units lack particles of the slit and clay fraction, which are an essential component of debris flows. It can therefore be assumed that the conglomeratic sections of the Toro basin generally show less debris-flow activity as the material requirements are not fully met.

The interplay between tectonic deformation and fluvial incision shapes landscapes over long timescales. Viewed at a decadal timescale, the region surrounding Salta has been repeatedly affected by seismic activity in recent years (e.g. Scott et al. (2014)). Over the past 20 years, only little seismic activity has been recorded in the QdT itself. However, earthquakes have originated in the foreland and to the northwest of the basin (Figure 6.6). If and to what extent these events have triggered landslides within

6. Discussion

the Toro basin that could feed future debris flows is unknown, but it is conceivable that M 6.3 earthquakes may be responsible for pervasive rock fracturing that in turn increases the availability of debris-flow material. Seismic hazard needs to be included in the assessment of debris-flow risk in the Eastern Andean Cordillera as its location close to an active continental margin implies recurring seismic events that can trigger mass movements through shaking.

Finally, I investigated the aspect of slopes concerning its relation to debris-flow intensity. Humid winds that originate in the Amazon basin and the Atlantic transport moisture into the Toro basin from the east (Strecker et al., 2007). The funnel-shaped character of the narrow gorge may cause certain slopes to be more exposed to rainstorm events than others. I restrict this analysis to the lower part of the Toro catchment, where this effect would be most pronounced and where the effect of greater moisture availability can also be recognized in the more pronounced vegetation cover (Figure 6.2 A). Aspect and intensity values are again extracted and averaged to sample points that have a more narrow spacing of 100 m and a buffer of 50 m to account for more spatial variability. This approach suggests higher debris-flow intensities at aspects of $340 - 60^\circ$ (Figure 6.7). North facing slopes are, however, generally rare across the lower QdT, which likely biases these results. Yet, the higher debris-flow intensities along more east-facing slopes could very well be a result of more pronounced rainstorm events, compared to slopes with an opposite orientation that would be more shielded.

Overall, steep-sloping topography generated by ongoing tectonic activity seems to be the main driver of debris-flow activity within the QdT. Additionally, the widely exposed Puncoviscana formation offers great amounts of cataclized material, that can easily be transported downhill if enough water is available. The requisite moisture is mostly available in the southern parts of the QdT, where I detect the highest debris-flow intensities. Heavy rainstorm events are needed for rainfall to be transported into the northern reaches of the Toro basin, which only occur during the wet season from December to February (Castino et al., 2017). With its steep gradients in topography and rainfall, the QdT serves as an excellent example for studying promotive factors of slope movement. The correlation between debris-flow intensity and different environmental conditions show unequivocally that various influences must be taken into account to explain the triggering of debris flow.

7. Conclusion

The geomorphological analyses based on high-resolution DEMs performed in this study reveal that the deeply entrenched river gorge and the steep-sloping eastern flank of the Toro catchment are primary initiation areas for debris flows. Infrastructure built in these sectors is particularly exposed to hazards related to slope movements. The major driver of debris-flow activity in the QdT is topographic slope associated with active fault segments. The extensive exposure of pervasively sheared meta-sediments of the Puncoviscana formation constitutes ideal lithologic conditions. Minimal debris-flow risk is associated with the low-sloping upper reaches of the Toro catchment and areas with a thick vegetation cover, which prevents occasional extreme rainfall events from efficiently removing and transporting large amounts of talus downhill.

Debris-flow incision imprints a characteristic topographic signature on the landscape, marked by channel gradients close to zero. This unique feature can be employed to distinguish between dominating hillslope processes, as it is very different from the slope-area relationship of fluvial channels. Basins within the QdT generally show topographic signatures associated with either fluvial or debris flow incision, or a mixture of both, leading to a curved slope-drainage area relation in loglog space. The $\log S \log A$ relation of a catchment not only provides information on the presence of debris flows. Identification of the transition zone between debris flow and fluvially dominated parts of the catchment through breakpoint detection can be applied to locate debris flows in 2D space. My approach to debris-flow recognition is relatively simple, fast, and applicable for hazard assessment at the regional scale, as it requires topographic information only. Applicability is merely limited by DEM resolution as higher scatter obscures geomorphic characteristics, which impedes the discrimination between individual basin types. Results from TanDEM-X data with a 12 m resolution are sufficiently good to allow this kind of qualification and differentiation of surface processes. Higher-resolution products are, however, preferable for more accurate debris-flow detection.

In high-relief areas, stereogrammetry is a viable tool for obtaining high-resolution surface models that show significantly fewer errors than publicly available elevation data. Optimal results require several pre- and post-processing steps in which map-

7. Conclusion

projecting stereo imagery onto a preexisting smooth surface is the most important one. The extent to which ground-control data can improve DEM quality needs to be explored further. As the ground-control data available for the QdT is spatially limited, I can only use part of their potential. Yet, indications for ground-truth related improvement of spatial coherence and internal consistency exists.

High-resolution remote sensing data are increasingly becoming available. I suggest that elevation models derived from stereo satellite imagery hold great potential for geomorphologic analyses at the meter scale. Stereo DEMs enable surveying of hillslope processes, such as debris flows, in high-relief regions where field access is generally difficult with limited distortions from rugged topography. Using high-resolution topographic data, I provide further evidence for the distinctive topographic signature of debris flows from NW Argentina and contribute to a better understanding of the relationships between the impact of extreme rainfalls at high elevation and the formation of large volumes of sediment in the arid highlands of the Andes.

A. Appendix

A.1. Peculiarities of topographic signatures from different catchment types

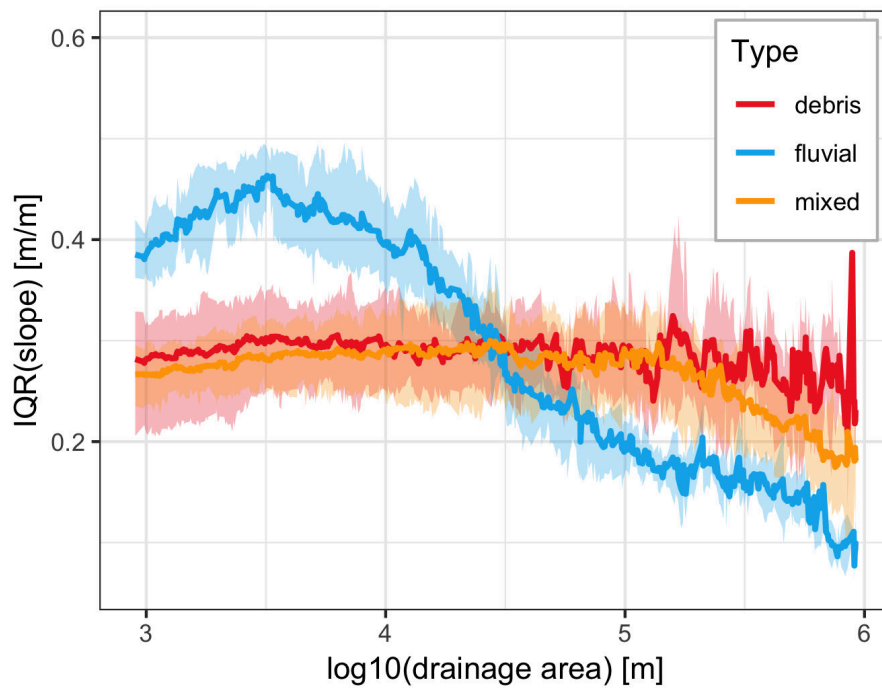


Figure A.1.: Aggregated mean IQR of slope within drainage-area logbins for hand-classified basins with topographic information extracted from ASP DEM.

High-resolution topographic data not only allows precise assessment of variations in topographic signature but has the potential to reveal further characteristics that are unique to different basin types. One particular thing that I noticed is the unique shape that arises when plotting the interquartile range (IQR) of topographic slope against drainage area. For all test basins exhibiting a clear, linear $\log S \log A$ relationship, the IQR showed a bulge with higher values at drainage areas around 3000 m^2 (Figure A.1 A). It implies that for fluvial catchments only, there is a greater

A. Appendix

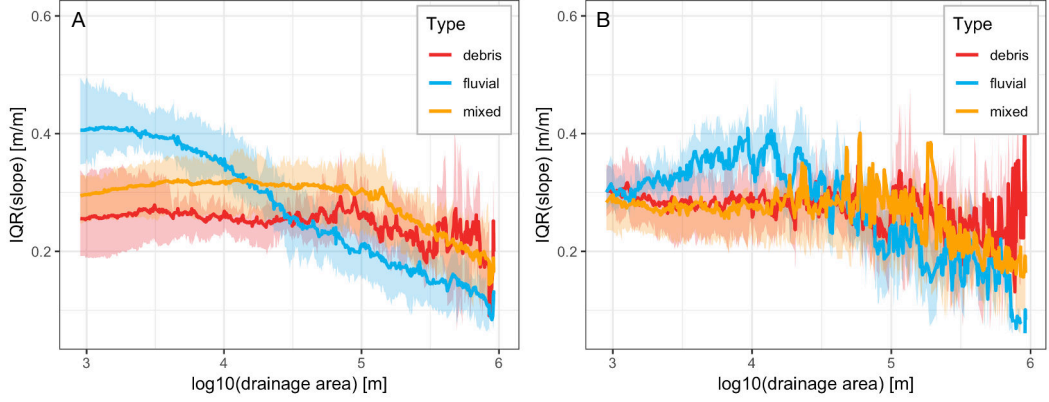


Figure A.2.: Aggregated mean IQR of slope within drainage-area logbins for auto-classified squares with topographic information extracted from ASP DEM (A) and IQR of hand-classified basins based on TanDEM-x data (B). Shaded areas indicate IQR of aggregated values.

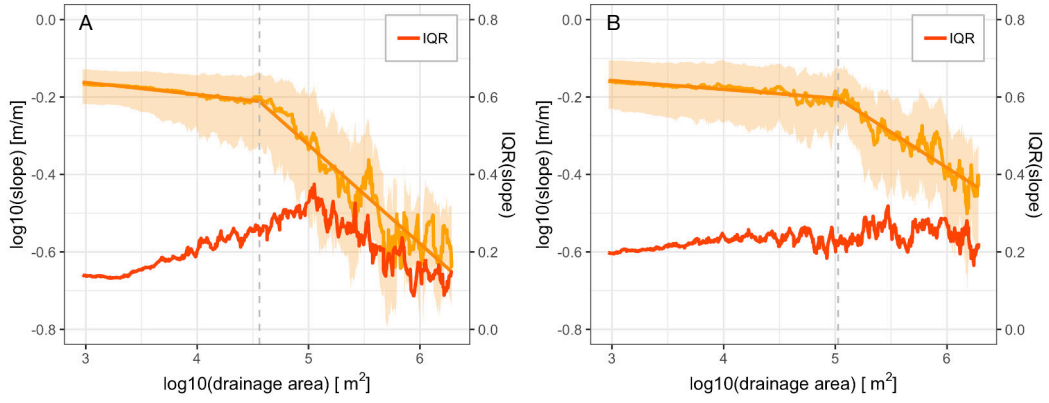


Figure A.3.: Log S log A relation and IQR of two exemplary test basins.

variety in slopes at small drainage areas. This peculiar IQR signal does not attribute to the fact that fluvial basins are, in general, more extensive, as it also manifests when investigating equally sized squares (Figure A.2 A). It is, however, only well observable using high-resolution data, as increasing scatter obscures the signal with increasing pixel size (see Figure A.2 B). It came to mind that the higher IQR signal could potentially be associated with the transition zone between debris flow and fluvial hillslope processes, which is found at small drainage areas for fluvial basins. Therefore, I would also expect to see an increased IQR in basins of type *mixed* close to the estimated breakpoint. A signal like this is lost when using an aggregational

A. Appendix

approach, as seen in Figure A.1 B, because the potential IQR bulge would be located at different drainage areas. To test this hypothesis, I look at individual basins, exhibiting topographic signatures of both debris flows and fluvial incision. The proposed relationship between breakpoint and IQR bulge works indeed for some basins (Figure A.3 A), but does not seem to be universally valid (Figure A.3 B). Hence, I abstain from further discussing this phenomenon in this study as there is not enough evidence to support a precise interpretation.

A.2. Further assessment of DEM quality

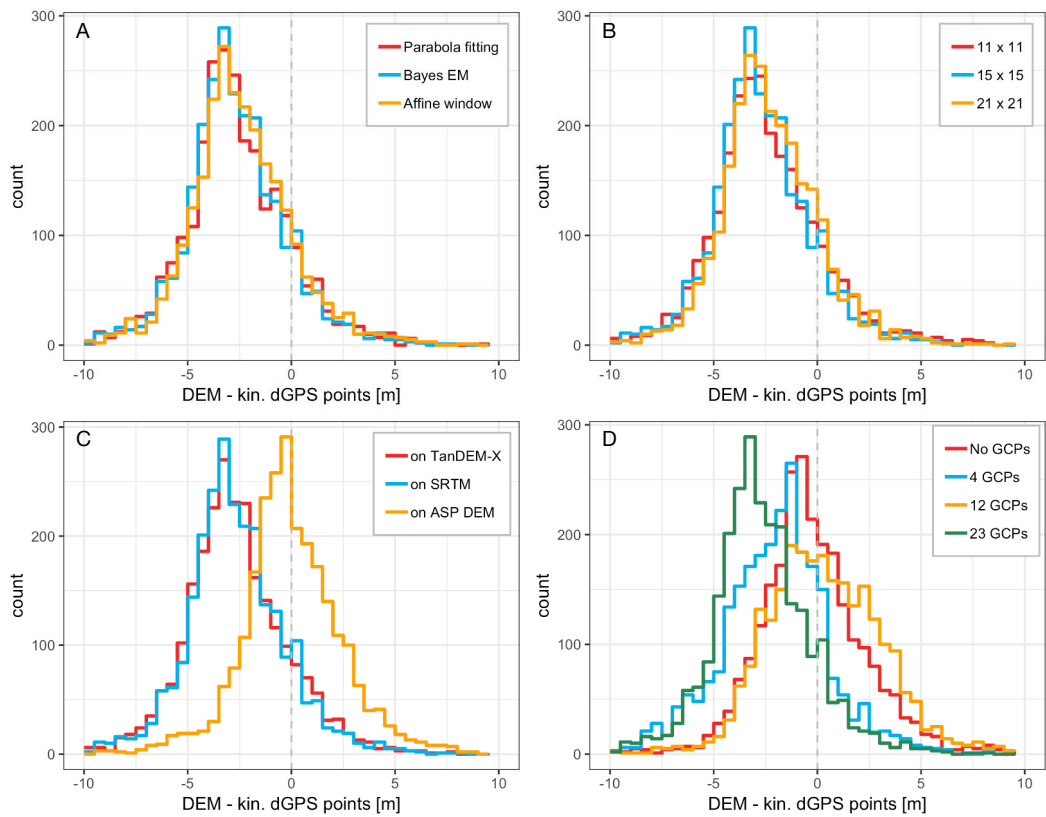


Figure A.4.: Difference of stereo DEMs to kinematic dGPS points, comparing subpixel-mode (A), subpixel kernel (B), reference DEM for map-projection (C), and number of GCPs used for bundle adjustment (D).

Visual assessment is the preferable method for quality control when evaluating the effect of differently sized correlation kernels and subpixel refinement modes, as coarseness does not affect the elevation of the model by much. This becomes evident

A. Appendix

when comparing different DEMs to the ground-control dataset (Figure A.4 A, B). Heights are more severely impacted by the choice of ground-control points in bundle adjustment and the reference DEM used for map-projection (Figure A.4 C, D). Very striking is the excellent correspondence between the DEM map-projected onto a smooth surface created from the SPOT-7 data itself and the ground-control points. Projection onto SRTM or TanDEM-X produces an offset of about three meters to the ground control. I conclude that the heights of the reference DEM are incorporated and thus have a lasting influence on the elevation of the final DEM. This implication needs to be considered when employing publicly available DEMs during map-projection since they might not provide very accurate elevation data in high-relief areas. For a more reliable representation of surface elevation, alignment to ground-control data is inevitable.

Ground-control points for bundle adjustment should be applied with care. Figure A.4 D reveals that the result of very few points is similar to the DEM produced without any field measurements. Increasing this number, however, leads to a greater spread when comparing the resulting DEM to ground control. Only when I employ all available ground-control points, the height distribution becomes narrower again. It is reasonable to assume that additional ground-control points spread over a larger area will further enhance the results. The availability of ground-control data will, however, always be limited by the accessibility of the respective study area.

A.3. DEMs from Cartosat-1

The quality of DEMs generated with Cartosat data is far below that of SPOT-7 DEMs (Figure A.3). Deeply incised river valleys are particularly difficult to map, resulting in holes in the elevation model. This makes the DEMs unsuitable for analyzing debris-flow activity. The poor DEM quality attributes partly to the coarser spatial resolution of 2.5 m, and most importantly to the fact Cartosat-1 only provides stereo pairs, whereas SPOT-7 offers tri-stereo data. Surface observation from multiple angles is crucial to depict all facets of high-relief terrain. Cartosat-1 data may provide better results for DEM generation on more even terrain.

A. Appendix

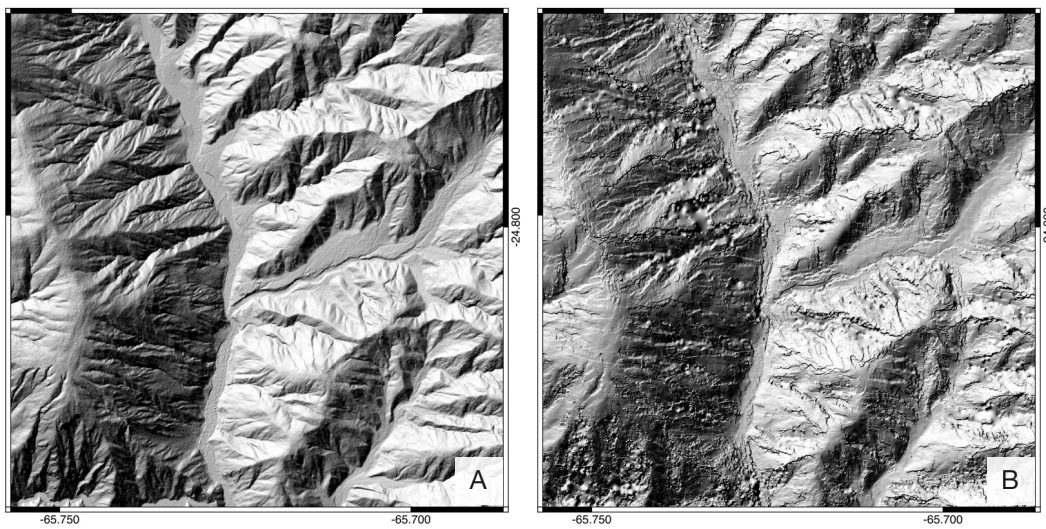


Figure A.5.: Visual assessment of DEM created from SPOT-7 data (A) compared to results from Cartosat-1 (B), generated with the same input parameters for stereo correlation.

Bibliography

- Baddeley, A. J., Turner, R., et al. (2004). Spatstat: An r package for analyzing spatial point patterns.
- Beyer, R. A., Alexandrov, O., and McMichael, S. (2018). The ames stereo pipeline: Nasa's open source software for deriving and processing terrain data. *Earth and Space Science*, 5(9):537–548.
- Castino, F., Bookhagen, B., and Strecker, M. (2017). Rainfall variability and trends of the past six decades (1950–2014) in the subtropical nw argentine andes. *Climate Dynamics*, 48(3-4):1049–1067.
- Cencetti, C. and Rivelli, F. (2011). Landslides dams induced by debris flows in quebrada del toro (province of salta, argentina). In *5th International Conference on Debris-Flow Hazards Mitigation: Mechanics, Prediction and Assessment*, pages 645–650.
- Chen, X., Sun, Q., and Hu, J. (2018). Generation of complete sar geometric distortion maps based on dem and neighbor gradient algorithm. *Applied Sciences*, 8(11):2206.
- Collison, A. and Anderson, M. (1996). Using a combined slope hydrology/stability model to identify suitable conditions for landslide prevention by vegetation in the humid tropics. *Earth surface processes and landforms*, 21(8):737–747.
- Costa, J. E. (1984). Physical geomorphology of debris flows. In *Developments and applications of geomorphology*, pages 268–317. Springer.
- Flint, J.-J. (1974). Stream gradient as a function of order, magnitude, and discharge. *Water Resources Research*, 10(5):969–973.
- García, V. H., Hongn, F., Yagupsky, D., Pingel, H., Kinnaird, T., Winocur, D., Cristallini, E., Robinson, R. A., and Strecker, M. R. (2019). Late quaternary tectonics controlled by fault reactivation. insights from a local transpressional system in the intermontane lerma valley, cordillera oriental, nw argentina. *Journal of Structural Geology*, 128:103875.

Bibliography

- Hilley, G. E. and Strecker, M. R. (2005). Processes of oscillatory basin filling and excavation in a tectonically active orogen: Quebrada del toro basin, nw argentina. *Geological Society of America Bulletin*, 117(7-8):887–901.
- Iverson, R. M. (1997). The physics of debris flows. *Reviews of geophysics*, 35(3):245–296.
- Iverson, R. M. and Reid, M. E. (1992). Gravity-driven groundwater flow and slope failure potential: 1. elastic effective-stress model. *Water Resources Research*, 28(3):925–938.
- Jarvis, A., Reuter, H. I., Nelson, A., Guevara, E., et al. (2008). Hole-filled srtm for the globe version 4, available from the cgiar-csi srtm 90m database.
- Ježek, P., Willner, A. P., Aceñolaza, F. G., and Miller, H. (1985). The puncoviscana trough—a large basin of late precambrian to early cambrian age on the pacific edge of the brazilian shield. *Geologische Rundschau*, 74(3):573–584.
- Klubertanz, G., Laloui, L., and Vulliet, L. (2009). Identification of mechanisms for landslide type initiation of debris flows. *Engineering geology*, 109(1-2):114–123.
- Loghin, A.-M., Otepka, J., and Karel, W. (2019). Accuracy analysis of digital elevation models from very high resolution satellite imagery. *Publikationen der DGPF*, Band 28.
- Marrett, R. and Strecker, M. R. (2000). Response of intracontinental deformation in the central andes to late cenozoic reorganization of south american plate motions. *Tectonics*, 19(3):452–467.
- Montgomery, D. R. and Foufoula-Georgiou, E. (1993). Channel network source representation using digital elevation models. *Water Resources Research*, 29(12):3925–3934.
- Muggeo, V. M. (2003). Estimating regression models with unknown break-points. *Statistics in medicine*, 22(19):3055–3071.
- Muggeo, V. M. et al. (2008). Segmented: an r package to fit regression models with broken-line relationships. *R news*, 8(1):20–25.
- Nelson, A., Reuter, H., and Gessler, P. (2009). Dem production methods and sources. *Developments in soil science*, 33:65–85.

Bibliography

- Santos, R. and Duarte, R. M. (2006). Topographic signature of debris flow dominated channels: implications for hazard assessment. *WIT Transactions on Ecology and the Environment*, 90.
- Scott, C., Lohman, R., Pritchard, M., Alvarado, P., and Sánchez, G. (2014). Andean earthquakes triggered by the 2010 maule, chile (mw 8.8) earthquake: Comparisons of geodetic, seismic and geologic constraints. *Journal of South American Earth Sciences*, 50:27–39.
- Seidl, M. and Dietrich, W. (1992). The problem of bedrock channel erosion. *Catena Suppl*, 23:101–124.
- Shean, D. E., Joughin, I. R., Dutrieux, P., Smith, B. E., and Berthier, E. (2019). Ice shelf basal melt rates from a high-resolution digital elevation model (dem) record for pine island glacier, antarctica. *The Cryosphere*, 13(10):2633–2656.
- Stock, J. and Dietrich, W. E. (2003). Valley incision by debris flows: Evidence of a topographic signature. *Water Resources Research*, 39(4).
- Stock, J. D. and Dietrich, W. E. (2006). Erosion of steepland valleys by debris flows. *Geological Society of America Bulletin*, 118(9-10):1125–1148.
- Stock, J. D., Montgomery, D. R., Collins, B. D., Dietrich, W. E., and Sklar, L. (2005). Field measurements of incision rates following bedrock exposure: Implications for process controls on the long profiles of valleys cut by rivers and debris flows. *Geological Society of America Bulletin*, 117(1-2):174–194.
- Strecker, M., Alonso, R., Bookhagen, B., Carrapa, B., Hilley, G., Sobel, E., and Trauth, M. (2007). Tectonics and climate of the southern central andes. *Annu. Rev. Earth Planet. Sci.*, 35:747–787.
- Takahashi, T. (1981). Debris flow. *Annual review of fluid mechanics*, 13(1):57–77.
- Tang, C., Zhu, J., Li, W., and Liang, J. (2009). Rainfall-triggered debris flows following the wenchuan earthquake. *Bulletin of Engineering Geology and the Environment*, 68(2):187–194.
- Tao, Y., Muller, J.-P., Sidiropoulos, P., Xiong, S.-T., Putri, A., Walter, S., Veitch-Michaelis, J., and Yerшов, V. (2018). Massive stereo-based dtm production for mars on cloud computers. *Planetary and Space Science*, 154:30–58.

Bibliography

- Tofelde, S., Schildgen, T. F., Savi, S., Pingel, H., Wickert, A. D., Bookhagen, B., Wittmann, H., Alonso, R. N., Cottle, J., and Strecker, M. R. (2017). 100 kyr fluvial cut-and-fill terrace cycles since the middle pleistocene in the southern central andes, nw argentina. *Earth and Planetary Science Letters*, 473:141–153.
- Wayne, W. J. (2011). Mass wasting as a geologic hazard in the province of salta, argentina. *Papers in the Earth and Atmospheric Sciences*.